Investigation of the Dielectric Properties and Microstructure of Al_2O_3-TiO_2 Microwave Ceramics

Yuting Xiao

Investigation of the Dielectric Properties and Microstructure of Al_2O_3-TiO_2 Microwave Ceramics

Research Thesis

In Partial Fulfillment of the
Requirements for the Degree of
Master of Science in Materials Engineering

Yuting Xiao

Submitted to the Senate of the Technion-Israel Institute of Technology

Kislev 5785 Haifa December 2024

The research thesis was done under the supervision of **Prof. W.D. Kaplan and Prof. Daniel Q. Tan** in the Department of Materials Science & Engineering, in Haifa, Israel and Shantou, China, respectively.

The generous financial support of Li Ka Shing Foundation Cross Disciplinary Research Grant, the Guangdong Provincial Key Laboratory of Materials and Technologies for Energy Conversion, and Guangdong Province Science and Technology Department Fund to Prof. Daniel Q. Tan is gratefully acknowledged.

The author of this thesis states that the research, including the collection, processing and presentation of data, addressing and comparing to previous research, etc., was done entirely in an honest way, as expected from scientific research that is conducted according to the ethical standards of the academic world. Also, reporting the research and its results in this thesis was done in an honest and complete manner, according to the same standards.

Table of Contents

Table of Contents I

List of Figures IV

List of Tables VII

Abstract 1

List of Symbols and Abbreviations 2

1. Literature Survey 4

1.1 Microwave Dielectric Ceramics 4

1.2 Basic MW Properties 5

1.2.1 Dielectric Permittivity 6

1.2.2 Quality Factor 7

1.2.3 Temperature Coefficient of Resonant Frequency 9

1.3 Hakki–Coleman Resonance Technique 10

1.3.1 Hakki–Coleman Resonance Technique 10

1.3.2 Split-post Dielectric Resonator Technique 11

1.3.3 Typical Alumina Dielectric Properties 12

1.4 Alumina 13

1.5 Solid State Sintering 15

1.6 Alumina-Titania System 16

1.6.1 Solid State Reaction 16

1.6.2 Dielectric Properties 18

2. Research Goals 20

3. Experimental Methods 21

3.1 Sample Processing 21

3.1.1 Al_2O_3-TiO_2 21

3.1.2 Al_2O_3-TiO_2 with Other Dopants 22

3.1.3 Al_2O_3-TiO_2 for SPDR Measurement 23
3.1.4 Sample Preparation for XRD and SEM 23
3.2 Characterization 24
3.2.1 Density 24
3.2.2 X-Ray Diffraction 24
3.2.3 Differential Scanning Calorimetry 24
3.2.4 Thermo-Gravimetric Analysis 24
3.2.5 Particle Size Analyzer. 25
3.2.6 Scanning Electron Microscopy 25
3.2.7 Dielectric Properties 25
4. Results and Discussion 26
4.1 The Influence of Titania 26
4.1.1 Density 26
4.1.2 Dielectric Properties 27
4.1.3 Characterization 30
4.2 Annealing Treatment Effect 31
4.2.1 Dielectric Properties 31
4.2.2 Characterization 34
4.3 Powder Processing Method Effect 38
4.4 Alumina Precursor Effect 40
4.4.1 Particle Size 40
4.4.2 Particle Size Distribution 41
4.4.3 Phases 43
4.5 Other Dopant Effect 44
4.5.1 Al_2O_3-TiO_2-Nb_2O_5/ Mn_2O_3-$BaZrO_3$-ZnO 44
4.5.2 Bi_2O_3 Dopant 45
4.5.3 MgO Dopant 46

4.6 Dielectric Properties at 10 GHz 47

5. Summary and Conclusions 50

6. Future Work 51

7. References 52

List of Figures

Figure 1 : The interaction of electric and magnetic field lines with a cylindrical ceramic resonator, as described by Richtmyer [2]. 4

Figure 2 : Applications of MWDCs in different frequencies, as plotted by Hongcheng [4]. 5

Figure 3 : Schematic showing a resonant peak and associated parameters [1]. 8

Figure 4 : Hakki–Coleman resonance technique. 11

Figure 5 : Split-post dielectric resonator technique. 12

Figure 6 : Schematic drawing of the hexagonal (a) and rhombohedral (b) unit cells of α-alumina. The blue spheres represent aluminum cations, and the red spheres represent oxygen anions [39]. 14

Figure 7 : Phase transformation of alumina [40]. 14

Figure 8 : Basic phenomena occurring during sintering under the driving force for sintering [41]. 16

Figure 9 : The phase diagram of Al_2O_3–TiO_2 [44]. 17

Figure 10 : Schematic diagram of the formation process of Al_2TiO_5 in Al_2O_3-TiO_2 system [44]. 17

Figure 11 : Relative density of Al_2O_3 - 5/7.5 wt% TiO_2 with respect to sintering temperature. 26

Figure 12 : SEM-SE image of Al_2O_3-7.5wt%TiO_2 sintered at 1300℃ for 4hrs (fracture). 27

Figure 13 : Permittivity of Al_2O_3 - 2.5/5/7.5/10 wt% TiO_2 with different sintering temperature. 28

Figure 14 : Qf of Al_2O_3 - 2.5/5/7.5/10 wt% TiO_2 with different sintering temperature. 28

Figure 15 : Permittivity of Al_2O_3 - 2.5/5/7.5/10 wt% TiO_2 with different sintering duration. 29

Figure 16 : Qf of Al_2O_3 - 2.5/5/7.5/10 wt% TiO_2 with different sintering duration. 29

Figure 17 : τ_f of Al_2O_3 – 0/2.5/5/7.5/10 wt% TiO_2 sintered at 1400℃ for 4 hrs. 30

Figure 18 : XRD curves of Al_2O_3 – 2.5/5/7.5/10 wt% TiO_2 sintered at 1400℃ for 4 hrs. 31

Figure 19 : Permittivity of Al_2O_3 - 2.5/5/7.5/10 wt% TiO_2 with different annealing duration. 32

Figure 20 : Qf of Al_2O_3 - 2.5/5/7.5/10 wt% TiO_2 with different annealing duration..... 32

Figure 21 : τ_f of Al_2O_3 - 2.5/5/7.5/10 wt% TiO_2 with different annealing duration..... 33

Figure 22 : τ_f of Al_2O_3 - 5 wt% TiO_2 with 0/2 hrs/5 hrs/10 hrs/15 hrs/24 hrs annealing. 33

Figure 23 : DSC of 1400℃ 4 hrs sintered Al_2O_3-7.5wt% TiO_2..... 34

Figure 24 : XRD curves of sintered Al_2O_3-7.5wt% TiO_2 sample with 1000℃ annealing temperature and different annealing time, the bottom is JCPDS of Al_2TiO_5..... 35

Figure 25 : BSE images of sintered Al_2O_3-7.5wt% TiO_2 sample with different annealing duration..... 35

Figure 26 : SEM-EDS images of as sintered Al_2O_3-7.5wt% TiO_2 sample. 36

Figure 27 : SEM-EDS images of the sintered Al_2O_3-7.5wt% TiO_2 sample annealed for 2 hrs. 37

Figure 28 : SEM-EDS images of the sintered Al_2O_3-7.5wt% TiO_2 sample annealed for 10 hrs. 37

Figure 29 : Qf of Al_2O_3(30nm, α+θ)-7.5wt% TiO_2 using different ways to processing raw powders. 38

Figure 30 : Density and Qf of Al_2O_3(30nm, α+θ)-7.5wt% TiO_2 with respect to ball milling duration. Samples were sintered at 1400℃ for 4 hrs. 39

Figure 31 : TGA curves of Al_2O_3(30nm, α+θ)-7.5wt% TiO_2 powder with different ball milling duration..... 39

Figure 32 : Density of sintered Al_2O_3-7.5wt% TiO_2 sample with different Al_2O_3 particle size and sintering temperature. 40

Figure 33 : Qf of sintered Al_2O_3-7.5wt% TiO_2 sample with different Al_2O_3 particle size and sintering temperature. 41

Figure 34 : Density and Qf of Al_2O_3-7.5wt% TiO_2 sample with different Al_2O_3 particle sizes which are sintered at 1400℃ for 4hrs. 444nm alumina is obtained using 150nm alumina heat treated at 1200℃ for 30min. The rest powders are commercial. 42

Figure 35 : Left: particle size distribution of 400nm powder. Right: particle size distribution of 1500nm-1200(d50=444nm) powder. 43

Figure 36 : XRD pattern of different alumina powders. 43

Figure 37 : Qf of Al_2O_3-7.5wt% TiO_2 with different alumina phases. 44

Figure 38 : Qf of 93.5wt% Al_2O_3-6.5wt% TiO_2-0.3wt% Nb_2O_5-0.5wt% $BaZrO_3$-0.25/0.5/0.75wt% ZnO (Without Mn_2O_3) and 93.5wt% Al_2O_3-6.5wt% TiO_2-0.3wt% Nb_2O_5-0.08wt% Mn_2O_3-0.5wt% $BaZrO_3$-0.25/0.5/0.75wt% ZnO (With Mn_2O_3) samples. 45

Figure 39 : Qf of Al_2O_3-7.5wt% TiO_2 adding Bi_2O_3 dopants. 46

Figure 40 : Permittivity of Al_2O_3 – 2.5/5/7.5/10 wt% TiO_2 measured by SPDR at 10GHz 48

Figure 41 : Dielectric loss of Al_2O_3 – 2.5/5/7.5/10 wt% TiO_2 measured by SPDR at 10GHz 48

List of Tables

Table 1 : Dielectric properties of alumina measured using various techniques. 13

Table 2 : Compositions of Al_2O_3-TiO_2 samples..... 21

Table 3 : Density and Qf of Al_2O_3-7.5wt% TiO_2 with MgO dopants sintered at 1400℃ for 4 hrs. 47

Abstract

Alumina (Al_2O_3) emerges as a promising candidate for millimeter-wave dielectric ceramics owing to its exceptional quality factor (Qf ~ 333,000 GHz), albeit constrained by its negative temperature coefficient of resonant frequency (τ_f ~ -60 ppm/°C) and relatively low dielectric constant (εr ~ 9.6). While previous studies employed TiO_2 (τ_f = +450 ppm/°C) for τ_f compensation, conventional formulations require excessive TiO_2 content (>8 wt.%) with compromised Qf values. This study systematically investigates Al_2O_3-TiO_2 composites (2.5-10 wt.% TiO_2) to determine the minimal dopant concentration maintaining optimal dielectric performance. Through comprehensive analysis of sintering behavior and post-annealing effects, we optimize microwave dielectric properties while elucidating the dual roles of TiO_2 additives and secondary Al_2TiO_5 phase formation.

Sintering submicron Al_2O_3 with 7.5 wt.% TiO_2 at 1400°C for 8 h achieved enhanced characteristics (εr = 10.73, Qf = 126,347 GHz @13.814 GHz), with subsequent annealing effectively stabilizing τ_f near zero. Thermal treatment induces Al_2TiO_5 decomposition into Al_2O_3 and TiO_2, accompanied by titanium redistribution. Comparative processing analysis identified high-speed rotation as the most effective mixing method. Extended evaluation of alumina precursors revealed that submicron particles with uniform phase distribution yield optimal performance.

Doping strategies 93.5wt% Al_2O_3-6.5wt% TiO_2-0.3wt% Nb_2O_5-0.08wt% Mn_2O_3-0.5wt% $BaZrO_3$-0.25/0.5/0.75wt% ZnO demonstrated significant potential for lowering sintering temperatures while enhancing dielectric properties. Multimodal characterization via X-ray diffraction, scanning electron microscopy, differential scanning calorimeters, thermo-gravimetric analysis, and dielectric measurements established microstructure-property correlations.

List of Symbols and Abbreviations

ε	Absolute dielectric permittivity
BSD	Backscatter diffraction
$℃$	Celsius degrees
ρ	Density
tanδ	Dielectric loss
DSC	Differential scanning calorimeters
D	Dry weight
EDS	Energy dispersive spectroscopy
α_L	Linear expansion coefficient
MW	Microwave
MWDCs	Microwave dielectric ceramics
PVA	Polyvinyl alcohol
Q	Quality factor
Qf	Quality factor multiplied by resonant frequency
S11	Reflected signal
ε_r	Relative permittivity
f_0	Resonant frequency
τ_f	Resonant frequency temperature coefficient
W	Saturated weight
SEM	Scanning electron microscopy
SE	Secondary electrons
l	Signal transmission distance
c	Speed of light in a vacuum
SPDR	Split-post dielectric resonator
S	Suspended weight
T	Temperature
τ_ε	Temperature coefficient of permittivity
TGA	Thermo-gravimetric analysis
t	Time
TEM	Transmission electron microscopy

S21	Transmitted signal
ε_0	Vacuum permittivity
XRD	X-ray diffraction

1. Literature Survey

1.1 Microwave Dielectric Ceramics

Wireless communication networks enable transmitting signals between cells using antennas mounted on masts and connected to base stations. Each base station contains microwave (MW) resonators that transmit signals of a specific frequency and remove or filter stray signals and sidebands that disrupt the quality of the transmission and reception frequencies.

The resonator's selectivity for frequency is of primary importance, so low dielectric loss ceramics are preferred to cheaper metal cavities [1] These ceramics are called Microwave dielectric ceramics (MWDCs). Cylindrical MWDC pucks, based on Richtmyer's original concept, first published in the 1930s, are designed for single-mode resonator applications [2]. **Figure 1** illustrates the interaction between the electric and magnetic field lines of electromagnetic (EM) radiation with the puck.

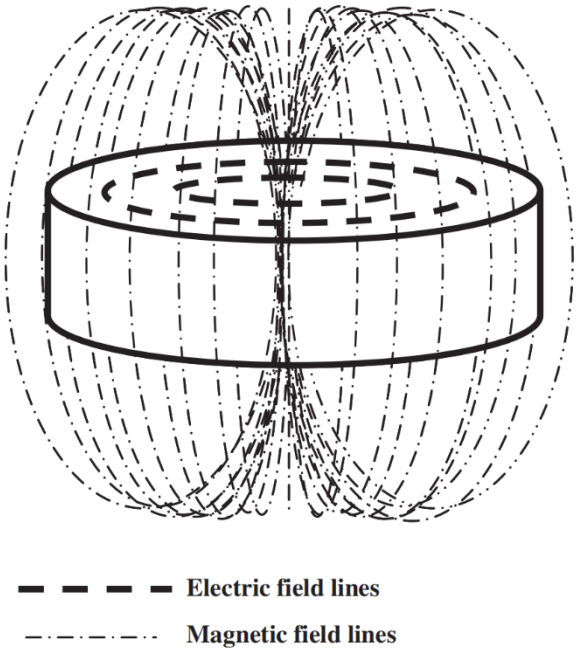

Figure 1: The interaction of electric and magnetic field lines with a cylindrical ceramic resonator, as described by Richtmyer [2].

This puck is designed to sustain a standing wave at a specific resonant frequency within its structure, allowing it to function as a filter or transmitting resonator [2]. However, the development of MWDCS has progressed slowly due to the lack of suitable materials for the

dielectric resonator. The breakthrough discovery of rutile (titanium dioxide) in the 1970s revolutionized the field, paving the way for the practical synthesis of dielectric resonators [3].

MWDCs are also utilized in RF antennas, frequency identifiers, radars, home satellite real-time TV receivers, and various other applications. The application of MWDCs in different frequencies is plotted in **Figure 2**.

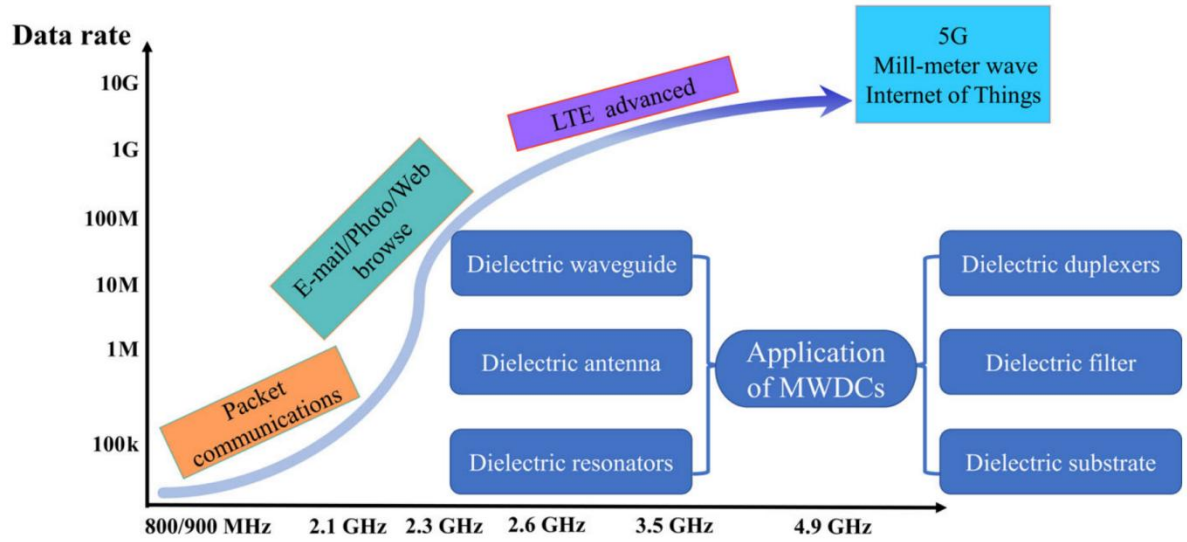

Figure 2: Applications of MWDCs in different frequencies, as plotted by Hongcheng [4].

Facing the challenges of 5G and forthcoming 6G, high speed, low delay more efficient, and reliable microwave dielectric ceramics are now required.

1.2 Basic MW Properties

To meet the stability, efficiency, and portability, a MWDCs candidate material has a suitable permittivity (ε_r), low dielectric loss (tanδ), and a near-zero resonant frequency temperature coefficient (τ_f). When adjusting the microwave dielectric properties, it is important to consider two main components: the external factors and the intrinsic properties. The external factors primarily involve the influence of the synthesis method and the raw materials used. MWDCs are typically prepared through solid-state sintering, and the conditions under which sintering occurs directly impact the microstructure and density of the ceramics. These factors, in turn, affect the microwave dielectric properties. Additionally, the size distribution, purity, non-stoichiometric ratios of the raw materials, the types of compounds involved, and any pretreatment based on their physicochemical properties are crucial for achieving optimal microwave dielectric performance.

1.2.1 Dielectric Permittivity

In electromagnetism, absolute permittivity (ε) measures the electric polarizability of a dielectric material. A material with high permittivity polarizes more in response to an applied electric field than a material with low permittivity, enabling it to store more energy. In research, we typically use the relative permittivity (ε_r), defined as the ratio of a substance's permittivity to the permittivity of free space.

Permittivity is connected with MWDCs' size limitations. The dimensions must be large enough for proper fabrication processing.

$$f_0 \approx \frac{c}{\lambda_d \sqrt{\varepsilon_r}} \approx \frac{c}{D\sqrt{\varepsilon_r}} \tag{1}$$

Where f_0 is the resonant frequency, c is the speed of light in a vacuum, λ_d is the wavelength of the standing wave when it propagates in a medium. D is the diameter of the resonator. The larger the permittivity, the smaller the dimension of the products, which makes the device portable. Permittivity is also related to the signal transmitted speed.

$$t_d = \frac{l\sqrt{\varepsilon_r}}{c} \tag{2}$$

Where t_d is the time delay, l is the signal transmission distance. The square root of permittivity is proportional to the signal's time delay. To shorten the time delay in information transition, permittivity should be as low as possible.

In microwave dielectric ceramics, the permittivity requirements vary depending on the application. When used in substrates for microwave integrated circuits, support components, and dielectric waveguide substrates, it’s important for the permittivity value to be as low as possible. This helps to reduce the capacitance between circuits and minimizes the signal propagation delay between chips. Conversely, when dielectric ceramics are used as dielectric resonators, a high ε is desirable. A smaller dielectric resonator size leads to a greater concentration of electromagnetic energy within the dielectric material, making it less susceptible to interference from the surrounding environment. This characteristic is beneficial for miniaturizing devices while maintaining high quality.

In 2006, Ohsato et al. highlighted the development direction of microwave dielectric materials, including high-quality low-εr ceramics for millimeter wave applications, high-quality high-εr ceramics for base station applications, and high-εr ceramics aimed at the miniaturization of mobile phones [5].

1.2.2 Quality Factor

When a dielectric is subjected to an electric field, some of the electrical energy is inevitably converted into heat energy. The rate at which energy is lost as heat is known as dielectric loss power, or simply dielectric loss, and it is often represented by the symbol tan(δ). Here, δ is the dielectric loss angle, which is the complementary angle to the angle between the current vector and the voltage vector in a dielectric when exposed to an alternating electric field.:

Dielectric loss is a crucial quality indicator for dielectrics, as it not only consumes electrical energy but also generates heat, leading to an increase in temperature. This rise in temperature can disrupt the regular operation of devices and may reduce their lifespan. Therefore, to achieve high-quality devices, it is essential to minimize dielectric loss as much as possible.

The reciprocal of the dielectric loss tangent, tan δ, is known as the quality factor, Q. This factor is defined as 2π times the ratio of the energy stored in the resonator to the energy lost during each cycle of electric field change. In the microwave frequency range, the Q value is associated with the frequency of the microwaves:

$$Q = \frac{\Delta f_0}{f_0} = \frac{1}{tan\delta} \approx \frac{\omega_r^2}{\gamma\omega} = \frac{\omega_r^2}{2\pi f\gamma} \tag{3}$$

Where Q is the quality factor, ω_r is the angular frequency of the transverse optical mode of lattice vibration; γ is the attenuation coefficient; ω is the angular frequency when the microwave frequency is f.

In practical applications, Q is defined as the ratio of the resonant frequency f_0 to the bandwidth Δf_0 measured at the resonant frequency, 3 dB below the maximum height. As shown in **Figure 3**, the larger the quality factor Q, the sharper the resonant peak, the more conducive to frequency selection, and the smaller the probability of interference at the required frequency [1].

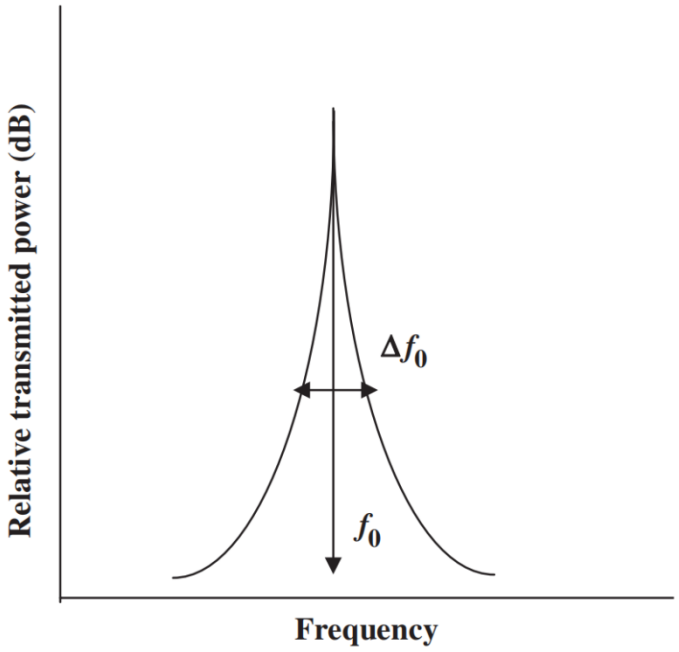

Figure 3: Schematic showing a resonant peak and associated parameters [1].

The formula 3 indicates that for microwave dielectric ceramics Q multiplied by f remains largely constant in the microwave range. As a result, the Qf value is commonly used to characterize the quality factor of a specific material. However, in practice, samples measured at higher frequencies, such as 5-10 GHz, tend to exhibit higher Qf values compared to the same material measured between 1-3 GHz. The exact reason for this discrepancy is not well understood, but it may be related to the processing conditions. Larger components, which resonate at lower frequencies, are statistically more likely to contain defects and flaws than smaller ceramic bodies [6]. The computation of the quality factor is given by [7, 8, 9, 10]:

$$\frac{1}{Q_L} = \frac{1}{Q_u} + \frac{1}{Q_{ext}} = \frac{1}{Q_d} + \frac{1}{Q_c} + \frac{1}{Q_r} + \frac{1}{Q_{ext}} \tag{4}$$

Where Q_L, Q_u, Q_{ext}, Q_d, Q_c, Q_r represent load, unload, external, dielectric, conductivity, and radiation quality factors, respectively.

Intrinsic losses represent the minimum losses that a system can achieve. They depend on factors such as crystal symmetry, frequency, and temperature. In contrast, extrinsic losses arise from structural order-disorder phase transitions and are associated with imperfections in the crystal lattice. These imperfections may include impurities, microstructural defects, grain boundaries, porosity, dislocations, vacancies, dopant atoms, processing conditions [11], order and disorder behavior [12, 13, 14, 15], etc.

Since actual crystals cannot be perfect, the non-intrinsic losses are typically much greater than the intrinsic losses. Consequently, these non-intrinsic losses primarily influence the dielectric material's quality factor. Therefore, minimizing non-intrinsic losses is a crucial objective for researchers aiming to improve the dielectric properties of materials.

1.2.3 Temperature Coefficient of Resonant Frequency

The resonant frequency temperature coefficient is a crucial indicator for assessing the stability of materials under temperature fluctuations. In practical applications, it is essential to select materials that have a resonant frequency temperature coefficient close to zero. This helps prevent the resonant frequency of microwave devices from drifting due to significant changes in the working temperature range, thereby ensuring the stability and accuracy of signal transmission. The principle for testing the resonant frequency temperature coefficient can be demonstrated as follows:

$$\tau_f = \frac{\Delta f}{f_0} \cdot \frac{1}{\Delta \mathrm{T}} = \frac{1}{f_0} \cdot \frac{f_T - f_0}{T - T_0} \tag{5}$$

where f_0 is the center of resonant frequency of the dielectric resonator at T_0 temperature, and f_T is the center of resonant frequency at T temperature. In most cases, T_0 is room temperature, and T is 85 degrees. The resonant frequency temperature coefficient is related to the linear expansion coefficient (α_L) and temperature coefficient of permittivity (τ_ε) as shown in the following formula:

$$\tau_f = -\left(\frac{\tau_\varepsilon}{2} + \alpha_L\right) \tag{6}$$

When τ_f is much larger than α_L, τ_f is approximately proportional to τ_ε. To adjust the material to obtain a near-zero resonant frequency, a composite method is usually adopted in actual engineering processes. That is, a positive resonant frequency temperature coefficient material is composited with a negative resonant frequency temperature coefficient material to achieve a near-zero resonant frequency temperature coefficient:

$$\tau_f = v_1 \tau_{f1} + v_2 \tau_{f2} \tag{7}$$

Where v_1 and v_2 are the volume fraction of two phases, and τ_{f1} and τ_{f2} are the τ_f value of two phases. In real practice, it is essential to maintain a small non-zero value of τ_f to compensate for the thermal expansion of the MW cavity effectively.

TCF is influenced by various factors, such as including the dielectric constant[16], phase transition[17, 18] and so on.

Alumina has a low dielectric permittivity and high Qf value, which means it has the advantages of fast transmission speed and good frequency selectivity, making it a favorable candidate for millimeter-wave applications.

1.3 Hakki–Coleman Resonance Technique

There are two primary techniques for measuring microwave properties: (i) transmission/reflection and (ii) resonance. The transmission/reflection technique effectively determines the real part of the dielectric constant for both high-loss and low-loss specimens, but it lacks the resolution needed to measure the low-loss tangent accurately. In contrast, the resonance technique is suitable only for low-loss materials, as an increase in loss causes the resonance curve to broaden. Generally, the resonance technique yields more accurate measurements of dielectric properties, especially in terms of loss. While transmission/reflection can sweep across a range of frequencies, resonance is limited to measuring at a specific frequency point [19, 20, 21, 22].

Resonance techniques are divided into two categories: cavity resonance methods and dielectric resonance methods. Although dielectric resonance techniques are more complex and require larger sample volumes, they are preferred for their enhanced accuracy in measuring dielectric properties. The differences among these techniques arise from the arrangement of metal shields and the type of signals measured, which can be either transmitted (S21) or reflected (S11). Transmission measurements employ weak coupling to minimize uncertainty, while reflection measurements utilize strong coupling [8, 23].

1.3.1 Hakki–Coleman Resonance Technique

One prominent method is the Hakki-Coleman resonance method, in which a cylindrical dielectric rod is positioned between two parallel metal plates, as shown in **Figure 4**. Power is

supplied via two coupling antennas, measuring the S21 parameter. The real part of the dielectric constant is determined based on the relationship between the resonant frequency and the dimensions of the sample [24, 25, 26, 27].

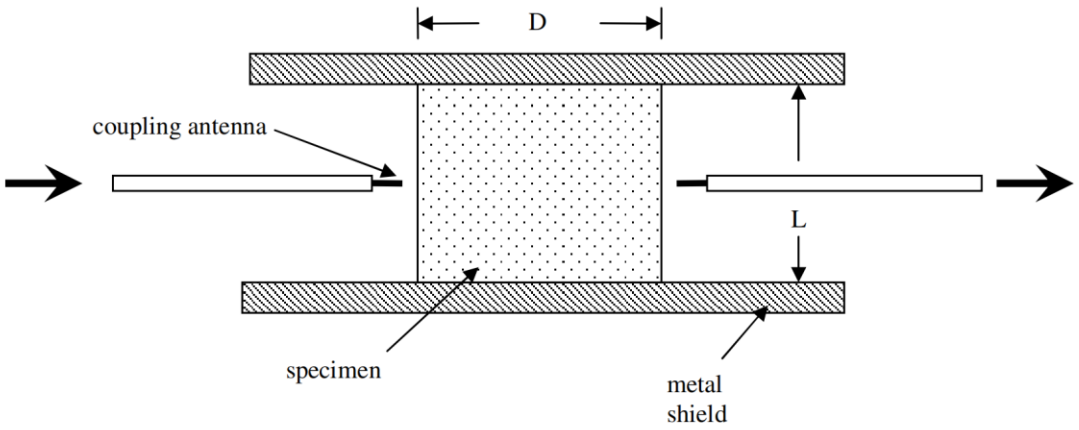

Figure 4: Hakki–Coleman resonance technique.

Accurately calculating the quality factor due to conductor loss is essential in the Hakki-Coleman method for precise loss tangent measurements. Typically, loss tangents can only be measured down to about 5×10^{-4} [24, 25]. If the surface resistance is precisely determined, the dielectric loss tangent values can be measured down to 1×10^{-4}.

The real part of permittivity is calculated by the dielectric/air boundary condition [24, 25, 26, 27]:

$$\frac{J_0(k_{ci}a)}{J_1(k_{ci}a)} = -\frac{k_{co}a}{k_{ci}a}\frac{K_0(k_{co}a)}{K_1(k_{co}a)} \tag{8}$$

where a is the radius of the sample, k_{ci} and k_{co} are the wavenumbers of r direction for r<a and r>a, respectively, and they are ε_r and sample geometry dependent. J and K are Bessel function and modified Bessel function, respectively.

1.3.2 Split-post Dielectric Resonator Technique

A very useful dielectric resonance method is the split-post dielectric resonator (SPDR) technique shown in **Figure 5**.

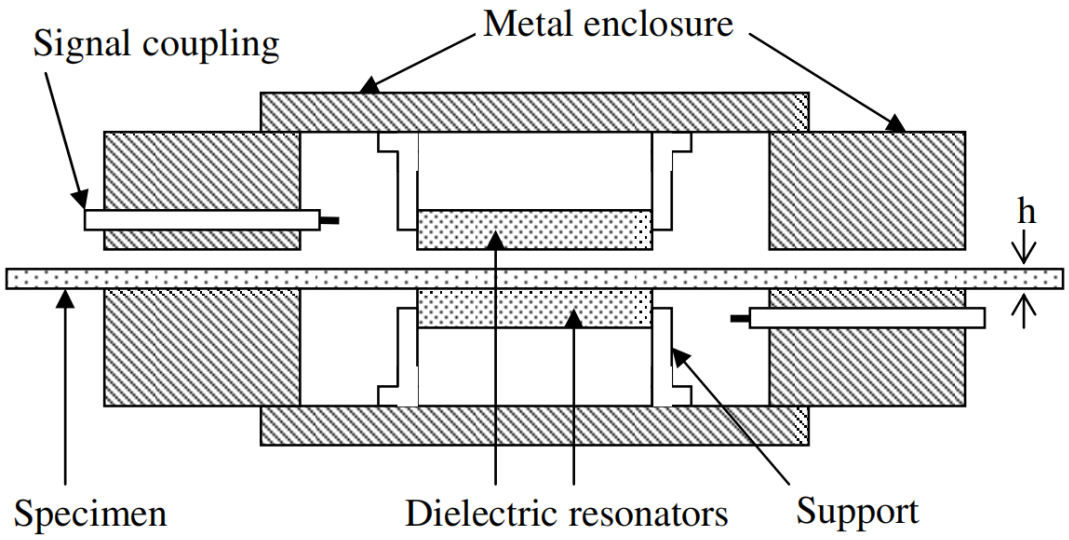

Figure 5: Split-post dielectric resonator technique.

This technique provides the highest accuracy for measuring real permittivity and enables the assessment of very low-loss materials that cannot be measured using other methods. Measuring at specific frequency points is usually sufficient, as lossless materials are nearly non-dispersive. This means that their dielectric constant and loss tangent remain relatively constant over a range of frequencies. The real part of the complex permittivity can be calculated using the following formula [9, 28, 29, 30]:

$$\varepsilon_r = 1 + \frac{f_0 - f_s}{h f_0 K_s(\varepsilon_r, h)} \tag{9}$$

Where h is the sample thickness, f_0 is the resonant frequency without the sample and f_s is the resonant frequency with the sample. K_s is a function of ε_r and h related. It has been pre-computed and tabulated for various ε_r and h values. Interpolation is then used to calculate K_s for specific permittivity and thickness values.

1.3.3 Typical Alumina Dielectric Properties

A list of the dielectric properties of alumina measured using various techniques, along with their standard deviations, is presented in Table 1.

Table 1: Dielectric properties of alumina measured using various techniques.

Techniques	Frequency(GHz)	ε_r	$tan\delta$	Refs
*S*11 and *S*21	0.05-18	~10	-	[31]
Cavity perturbation	8.2-12.4	9.9±0.4	Below measurement resolution	[32]
Hakki-Coleman	13.2	10.1±0.3	(1±0.4)×10⁻4	[32]
Cylindrical cavity	8.4	9.8±0.3	(6±1)×10⁻5	[32]
Others	10	10.15	8.4×10⁻6	[33]
Others	10	9.97	3.91×10⁻5	[31]
Others	10	9.5-10	3×10⁻4	[34]

The dielectric constants measured through various methods exhibit a high degree of consistency. In contrast, the loss tangent is significantly affected by manufacturing conditions, resulting in considerable discrepancies across published data. Remarkably, the loss tangent values obtained through the Hakki-Coleman technique are reasonable compared to those derived from cylindrical cavity and waveguide methods, primarily due to the higher resonant frequencies involved. Furthermore, at microwave frequencies, the loss tangent of ceramics typically increases with rising frequency [10, 35].

1.4 Alumina

Alumina (Al_2O_3) is a cost-effective and widely utilized inorganic material celebrated for its mechanical properties, particularly its hardness and compressive strength among oxides. Furthermore, alumina is an excellent insulator, showcasing high breakdown strength and electrical resistivity, making it one of the top insulating materials, surpassed only by SiO_2 [36, 37]. Alumina has a low dielectric permittivity, which is approximately 10, somewhat restricts its applications in electric capacitors and microwave resonators. Nonetheless, Al_2O_3 is of significant interest in microwave technology because sapphire, the single crystal form of the only thermodynamically stable structure of Al_2O_3, exhibits the lowest dielectric loss tangent among known substances. This means it has an extremely high quality factor value (Qf ~ 333,000GHz) [38]. This property enables the use of high-purity, non-porous, fine-grained Al_2O_3 in high-quality resonators, which are essential for low-noise oscillators.

Due to these attributes, it is popular in various fields. Alumina has many different phases, among which α-alumina (corundum form) is the thermodynamically stable phase of alumina. The structure of α-alumina is shown in **Figure 6**.

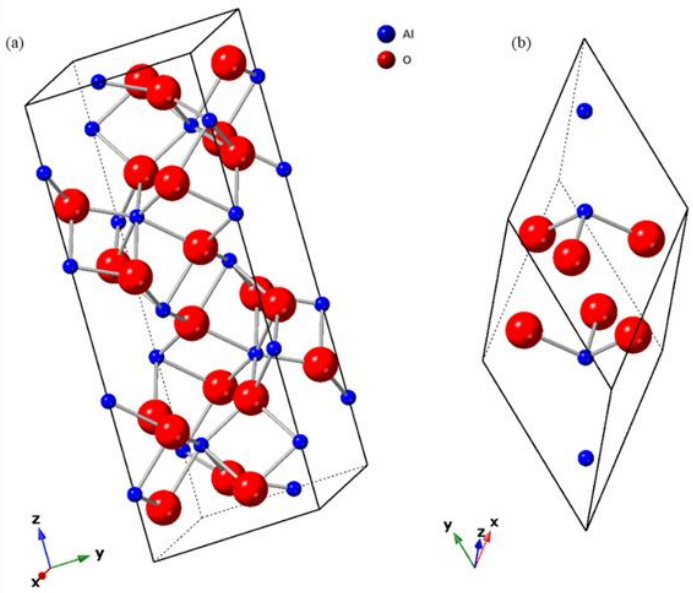

Figure 6: Schematic drawing of the hexagonal (a) and rhombohedral (b) unit cells of α-alumina. The blue spheres represent aluminum cations, and the red spheres represent oxygen anions [39].

The structures of aluminum oxide can continuously transform into one another through the kinetic paths shown in **Figure 7**:

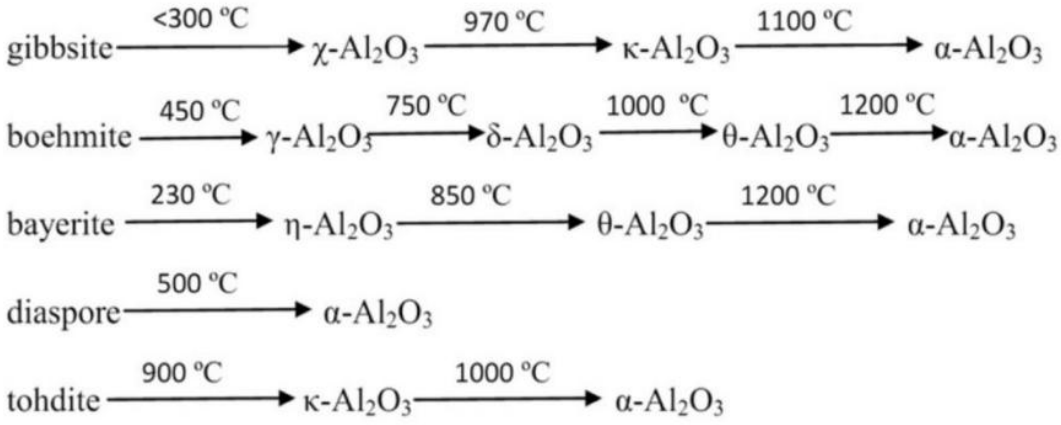

Figure 7: Phase transformation of alumina [40].

Usually, Alumina ceramics usually sintered at a high temperature above 1500 – 1800℃, which depends on powder particle size and environment. This means that the resulting dense ceramics will always be in the alpha alumina phase after sintering.

The incorporation of functional additives into Al_2O_3 serves as an approach to modulate its sintering behavior and performance. Specifically, TiO_2 promotes grain growth in Al_2O_3 and can balance τ_f of alumina. The mechanism will be elaborated in subsequent sections. Bi_2O_3 and Mn_2O_3, characterized by low melting points, effectively reduce alumina sintering temperatures through liquid-phase sintering mechanisms. Nb_2O_5 contributes to mechanical property enhancement, whereas MgO suppresses abnormal grain growth in corundum phases and promotes densification.

The particle size and crystalline phase of alumina precursors are critical determinants of final material properties. Notably, reducing alumina powder particle size significantly lowers the sintering temperature.

1.5 Solid State Sintering

Ceramics are typically manufactured through a sintering process, as it is challenging to reach temperatures above the melting point of most ceramic materials. Sintering is generally performed at a temperature range of $0.5T_m$ to $0.8T_m$, which allows for adequate atomic mobility. The primary motivation for sintering is to reduce the total surface and interfacial energy of the system [41]:

$$\Delta(\gamma A) = \Delta\gamma A + \gamma\Delta A \tag{10}$$

where γ is the total surface/interfacial energy, A is the total interface area and γA represents the total interfacial energy of a powder compact. The change in total surface energy, $\Delta\gamma$, is attributed to densification, while the change in interfacial area ΔA results from grain growth or grain coarsening. Densification and coarsening are competitive processes that can occur simultaneously, as presented schematically in **Figure 8**.

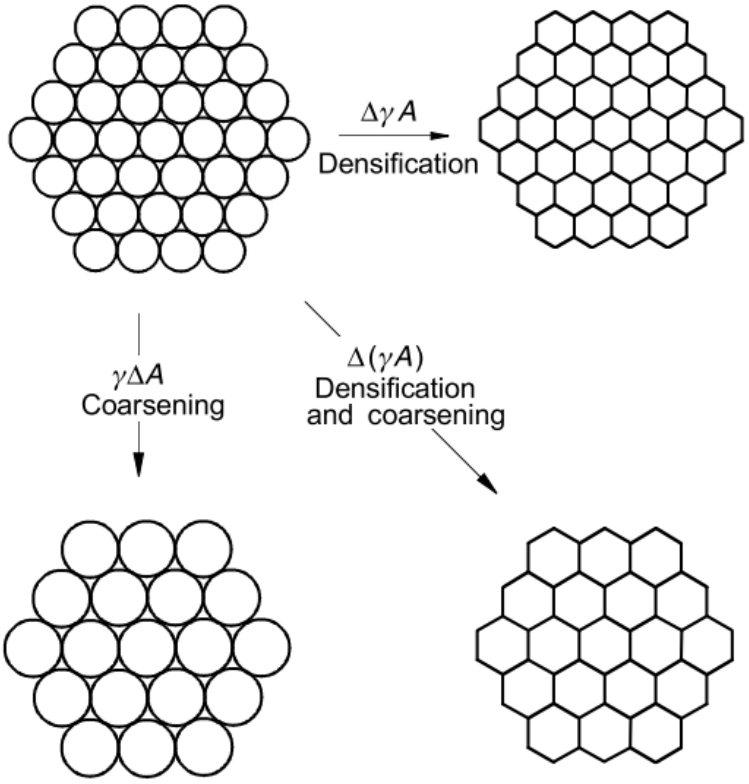

Figure 8: Basic phenomena occurring during sintering under the driving force for sintering [41].

In the sintering process, densification reduces pore size and enhances density, whereas coarsening results in the growth of both pores and particles. As a result, managing the sintering process remains a significant challenge within the ceramic industry.

1.6 Alumina-Titania System

1.6.1 Solid State Reaction

The initial sintering rate significantly increases with rising titania concentration, but levels off after reaching a certain threshold. This peak concentration is believed to correspond to the solubility limit of titania (TiO_2) in Al_2O_3 [42]. The solid solubility limit of TiO_2 in Al_2O_3 ranges between 0.20 and 0.24 wt% at 1520°C. TiO_2 in the amount of 0.25 wt% improves the dielectric properties of Al_2O_3 by reducing dielectric losses [43].

Figure 9 presents the phase diagram of Al_2O_3-TiO_2 [44]. Above 1283°C, the secondary phase Al_2TiO_5 will begin to form. The reaction can be expressed as [45]:

$$Al_2O_3(\alpha) + TiO_2(rutile) = Al_2TiO_5(\beta) \quad (11)$$

Al_2TiO_5 is metastable at low temperatures. Upon annealing at 900℃-1200℃, Al_2TiO_5 tends to decompose into Al_2O_3 and TiO_2 [46].

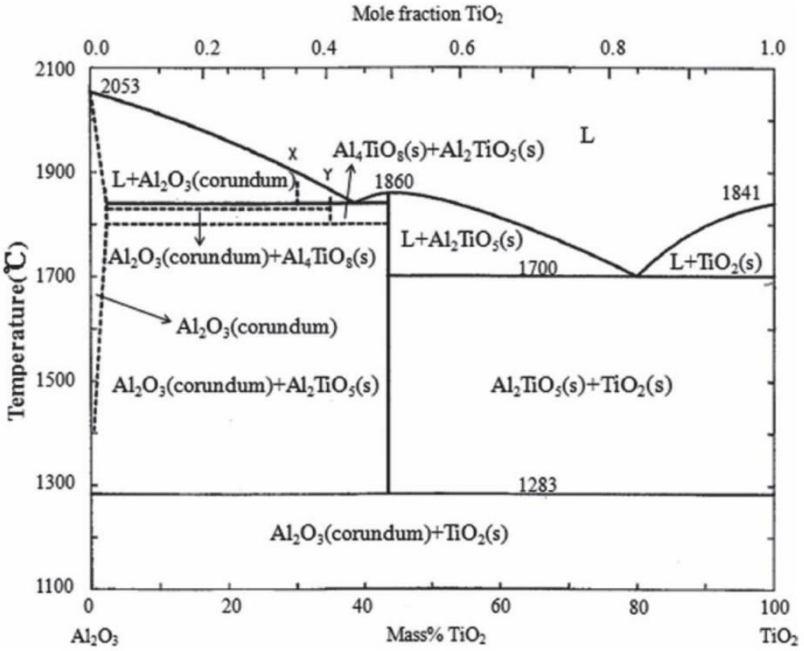

Figure 9: The phase diagram of Al_2O_3–TiO_2 [44].

The diffusion of Al^{3+} and Ti^{4+} ions is linked to the presence of vacancies. At high temperatures, the dissolution of Al^{3+} in TiO_2 and Ti^{4+} in Al_2O_3 generates vacancies [47, 48, 49, 50]. As illustrated in **Figure 10**, to maintain charge balance, one cation vacancy is created for every three Ti^{4+} ions that enter the Al_2O_3 structure.

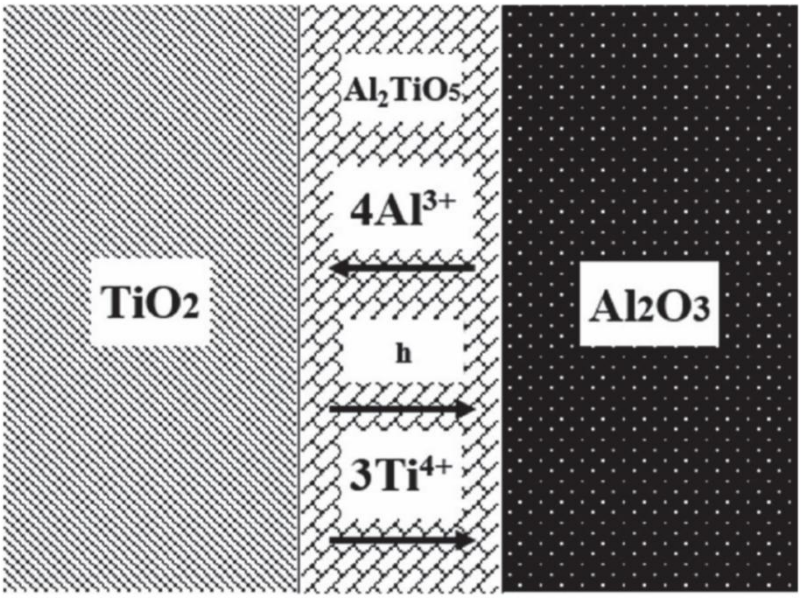

Figure 10: Schematic diagram of the formation process of Al_2TiO_5 in Al_2O_3-TiO_2 system [44].

The concentration of vacancies increases with temperature, facilitating ion movement. In the Al_2TiO_5 phase, the interdiffusion of Al^{3+} and Ti^{4+} ions occurs more frequently.

As the amount of titania additive approaches its solubility limit of 0.27 wt%, a notable increase in the density of alumina can be observed. However, when TiO_2 is added in excess beyond this soluble level, only a slight increase in density can be seen [51, 52]. The addition of 5 wt% and 10 wt% of titania reduces grain growth in alumina and suppresses intra-granular porosity. This effect occurs because the presence of the secondary phase inhibits grain growth through a pinning effect [51].

The addition of TiO_2 adversely impacts the dielectric loss of pure Al_2O_3, while the dual-phase system further disrupts the material's homogeneity. The formation of secondary phases during sintering complicates the microstructure evolution. So the TiO_2 content and processing conditions are crucial.

1.6.2 Dielectric Properties

As mentioned earlier, alumina holds potential for applications in microwave dielectrics due to its very negative τ_f value, which is close to -60. Introducing TiO_2 (τ_f=+450) into alumina to create a two-phase material can be an effective approach to bring the τf value closer to zero [53]. Researchers have conducted some work in this area, here are some samples:

i. Alford and Penn began investigating the combination of Al_2O_3 and TiO_2 to assess their dielectric properties [38]. They discovered that as the concentration of TiO_2 increased, the quality factor decreased significantly. For pure Al_2O_3, Qf is 333,000 GHz, while a composition with 10 wt% TiO_2 showed the Qf of remains 66,384 GHz.

ii. Ohishi et al. found that the formation of the secondary phase Al_2TiO_5 inhibited any improvement in the τ_f. even with a substantial addition of titanium. To address this issue, they employed low-temperature annealing to eliminate the secondary phase, achieving a near-zero τ_f; however, this process also resulted in a lower Qf [54].

iii. Campos et al. attempted to use lower sintering temperatures to avoid additional heat treatments and achieve a near-zero τ_f. Unfortunately, their ceramics lacked density, leading to unsatisfactory Qf values [55].

These studies collectively highlight a critical gap: no existing method simultaneously resolves the Qf-τ_f trade-off suppresses deleterious secondary phases and ensures high densification.

In this work, we transcend these limitations through several ways: (1) precision doping to identify a critical TiO_2 threshold that balances τ_f compensation with minimal Qf degradation; (2) dual-stage thermal engineering combining high-temperature sintering for densification with post-annealing to decompose Al_2TiO_5 and homogenize Ti distribution, thereby decoupling the Qf-τf conflict observed in prior studies; and (3) multi-component dopant design to lower sintering temperatures while enhancing dielectric properties.

2. Research Goals

This study focuses on the aluminum oxide-titanium oxide system with the primary goal of optimizing the dielectric properties of Al_2O_3-TiO_2 ceramics at microwave frequencies. Additionally, it aims to understand how microstructure affects these properties. Specifically, the research seeks to achieve the following objectives:

1. Identify the critical concentration of TiO_2 necessary to increase the Qf while maintaining the τ_f close to zero.
2. Enhance the dielectric properties of Al_2O_3-TiO_2 ceramics through further optimization of compositions and sintering profiles.
3. Elucidate the role of TiO_2 during heat treatment and its impact on phase transformations and the resulting properties of Al_2O_3.
4. Investigate the formation of secondary phases and their effects on the properties of the ceramics.
5. Analyze how the processing method, various alumina precursors, and dopants influence the dielectric properties of Al_2O_3-TiO_2 ceramics.

3. Experimental Methods

In this section, alumina processing routes, characterization methods, and methodology will be presented.

3.1 Sample Processing

3.1.1 Al_2O_3-TiO_2

Samples were prepared by mixing Al_2O_3 (99.99% purity) and TiO_2 (microsize, rutile, 99.99% purity). The raw materials and formula are shown in Table 2.

Table 2: Compositions of Al_2O_3-TiO_2 samples.

Formula		Al_2O_3 particle size	Al_2O_3 phase
Al_2O_3- x wt% TiO_2	X=2.5, 5, 7.5, 10	150nm	α
Al_2O_3-7.5wt% TiO_2		400nm	α
Al_2O_3-7.5wt% TiO_2		microsize	α
Al_2O_3-7.5wt% TiO_2		30nm	α+θ
Al_2O_3-7.5wt% TiO_2		30nm	γ

In addition to the ceramics listed in the table, pure alumina and titania ceramics were also produced for comparison.

The powder selection is aimed to balance particle size reduction for sintering temperature control with phase purity considerations, where ultrafine particles (30 nm) exhibit challenges in maintaining pure α-phase stability and tend to aggregate. This systematic investigation intended to evaluate these competing factors and identify optimal alumina precursor characteristics.

The Al_2O_3 and TiO_2 powders were weighed according to the stoichiometric ratios to obtain 30 grams of desired powder. 100 mL of ethanol was used to mix the powder in the form of a slurry. The slurry was loaded in a mixer (THINKY MIXER, Japan; MZ-8) and set the rotational speed to 1500 rpm and the rotation duration to 1 hour. After the slurry had been thoroughly mixed, it was transferred to a beaker and put in a 100-degree oven to dry for two days. Once the powder

dried, an agate grinding mortar was used to grind the powder. Binder was added at a ratio of 2 to 3 drops of a 5% Polyvinyl alcohol (PVA) solution for each gram of powder and then the mixture was sieved using a 100-mesh screen. A green body with a diameter of 12 mm was formed using 2 grams of powder, applying uniaxial pressure at 150 MPa. The pellets annealed in air at 600°C for 4 hours to remove the PVA and sintered at temperatures ranging from 1300°C to 1500°C for 2, 4, and 8 hours. For the samples sintered for 4 hours, an additional annealing process was conducted at 1000°C for 2 to 24 hours. All heat treatments were conducted in an air atmosphere at atmospheric pressure.

For the 30 nm Al_2O_3(α+θ phase)-7.5wt% TiO_2 and 150 nm Al_2O_3(α phase)-7.5wt% TiO_2 powders, ball milling was employed to mix the materials to investigate the effects of different powder processing methods on the samples. The general procedure remains consistent with previous methods. For 40 grams powder, 150 grams of 8 mm zirconia balls, 250 grams of 5 mm zirconia balls, and 150 grams of 3 mm zirconia balls were added. Additionally, 500 ml of deionized water was incorporated for mixing. Ball milling was carried out at a speed of 900 rpm for durations of 1, 4, 8, and 40 hours.

To eliminate agglomeration effects, powders consisting of Al_2O_3(α+θ phase)-7.5wt% TiO_2 and 150 nm Al_2O_3(α phase)-7.5wt% TiO_2 were deflocculated using a small amount of HCl. This was done to achieve a pH of approximately 4, which is significantly below the isoelectric point of Al_2O_3, facilitating deflocculation , [56, 57]. The mixed powders were formed through slip casting after being stirred for 5, 8, 16, and 24 hours. The other steps were the same as before.

3.1.2 Al_2O_3-TiO_2 with Other Dopants

The materials used in this research are 93.5wt% Al_2O_3-6.5wt% TiO_2-0.3wt% Nb_2O_5-0.5wt% $BaZrO_3$-0.25/0.5/0.75wt% ZnO and 93.5wt% Al_2O_3-6.5wt% TiO_2-0.3wt% Nb_2O_5-0.08wt% Mn_2O_3-0.5wt% $BaZrO_3$-0.25/0.5/0.75wt% ZnO. Al_2O_3-TiO_2. Raw materials were mixed by mixer. The subsequent steps of adding binder, sieving, pressing, sintering, etc. were the same as previous.

0.25 wt% and 1 wt% Bi_2O_3 was added into 150 nm Al_2O_3(α phase)-7.5wt% TiO_2 powder and homogenized using a mixer by wet mixing, and obtained the powder after drying. In addition

to direct mixing, an alternative method was employed. 10wt% Bi_2O_3 suspension was added into 150 nm Al_2O_3(α phase)-7.5wt% TiO_2 powder according to a ratio of three drops of the suspension per gram of powder. This mixture underwent thorough grinding and sieving. The green body was subsequently sintered at temperatures of 1200, 1250, 1350, 1400, 1450, and 1500 ℃ for four hours.

For the preparation of Mg-doped alumina samples, we combined 75 grams of high-purity α-Al_2O_3 powder with either 1 wt% or 2 wt% of $Mg(NO_3)_2 \cdot 6H_2O$, along with 150 grams of deionized water. We then added 30 drops of hydrochloric acid to achieve a pH of approximately 4, helping to prevent agglomeration. This mixture was blended for 24 hours to homolize Mg which was below the solubility limit in alumina.

3.1.3 Al_2O_3-TiO_2 for SPDR Measurement

SPDR can accurately detect the dielectric properties of materials at specific frequencies. However, there are strict requirements for the ceramics being measured: for a measurement at 10 GHz, the diameter of the sample must be larger than 25 mm, and the height should be approximately 0.7 mm. Preparing such large, thin ceramic discs can be challenging. The powder was mixed using mixer, and the green body was formed through uniaxial pressing at 100 MPa using 35mm die, followed by cold isostatic pressing at 250 MPa. After sintering, the sample thickness was reduced to meet the specified range by grinding.

3.1.4 Sample Preparation for XRD and SEM

For XRD measurements, the bulk samples were ground and polished using 180, 400, 800, and 2000 grit sandpaper to achieve a flat and smooth surface. After being thoroughly dried in an oven, these samples were ready for testing. Powder samples didn't require special processing; they only needed to be placed in a specific container, flattened, and compacted.

For scanning electron microscopy (SEM) measurements of the microstructure, the samples were polished and subsequently cleaned ultrasonically in ethanol for 30 minutes. Given the poor conductivity of aluminum oxide, the samples were wrapped in conductive tape, and silver paste was applied to enhance the conductive pathway. For SE/EDS detection, to further improve conductivity and mitigate charging effects on the sample surface, a thin layer of gold or carbon was sputtered onto the surface.

3.2 Characterization

3.2.1 Density

The density of samples ρ was determined using the Archimedes method following ASTM standard c 20-92:

$$\rho = \left(\frac{D}{W - S}\right) \cdot \frac{1}{\rho_{theoretical}} \tag{12}$$

where D is the dry weight, W is the saturated weight, S is the suspended weight and $\rho_{theoretical}$ is the theoretical density. The theoretical density of alumina is 3.98 gr/cm^3; alumina titanite is 3.73 gr/cm3, and titania is 4.23 gr/cm^3. Theoretical densities are calculated for samples of different compositions according to the formula.

3.2.2 X-Ray Diffraction

X-ray diffraction (XRD) was used for phase structure analysis of crystalline materials. Diffraction patterns were acquired at room temperature by a benchtop XRD system (MiniFlex 600, Rigaku Corporation). The scanning speed was 4°/min, the 2θ range was between 10° to 80°.

3.2.3 Differential Scanning Calorimetry

Differential Scanning Calorimeters (DSC) measure temperatures and heat flows associated with thermal transitions in a material. Properties measured by DSC techniques include glass transitions, “cold” crystallization, phase changes, melting, crystallization, product stability, cure/cure kinetics, and oxidative stability. In this research, DSC (TA discovery DSC 25) was used to examine the reaction between alumina and titania during the heat treatment.

3.2.4 Thermo-Gravimetric Analysis

Thermo-Gravimetric Analysis (TGA) is used to measure the relationship between sample mass and temperature or time under programmed temperature control. In this research, TGA (TA discovery TGA 55) was used to compare the differences between powders with different ball milling durations.

3.2.5 Particle Size Analyzer.

The particle size of powder was measured by a particle size analyzer (Brookhaven NanoBrook 90plus PALS), which is based on the dynamic light scattering technique.

3.2.6 Scanning Electron Microscopy

Scanning Electron Microscopy (SEM, Zeiss Gemini 450 and ThermoFisher Prisma E-SEM) was utilized to characterize the microstructure of alumina-based samples. The secondary electron (SE) mode of SEM provides high-resolution images of the sample surface, while the backscattered electron (BSE) mode reveals the atomic weight contrast and very limited surface topography information of the materials. Additionally, energy dispersive spectroscopy (EDS) was employed to analyze the distribution of elements within the samples.

3.2.7 Dielectric Properties

Permittivity, Qf and τ_f are measured using Hakki–Coleman resonance technique in GHz frequency range and Keysight ENA network analyzer. SPDR can be used to measure the dielectric properties at 10 GHz.

4. Results and Discussion

In this part, unless otherwise noted, the alumina powder used was 150 nm α phase alumina, the sintering temperature was 1400℃ and the sintering duration was 4 hrs.

4.1 The Influence of Titania

4.1.1 Density

Alumina has a relatively high melting temperature of approximately 2050℃. Due to its crystal structure and strong ionic bonds, the sintering temperature for alumina ceramics is generally relatively high compare with other ceramics applied in microwave dielectric field. Typically, the sintering temperature required to achieve 95% density in alumina ranges from 1500 to 1600 ℃.

From **Figure 11**, it is apparent that Al_2O_3 containing only 5 wt% TiO_2, when sintered at 1300℃, the relative density of sample exceeds 90%. When the TiO_2 content is increased to 7.5 wt% at the same sintering temperature, the relative density rises even higher, surpassing 93%, as further corroborated by **Figure 12**.

At a sintering temperature of 1350℃, both samples approach full densification.

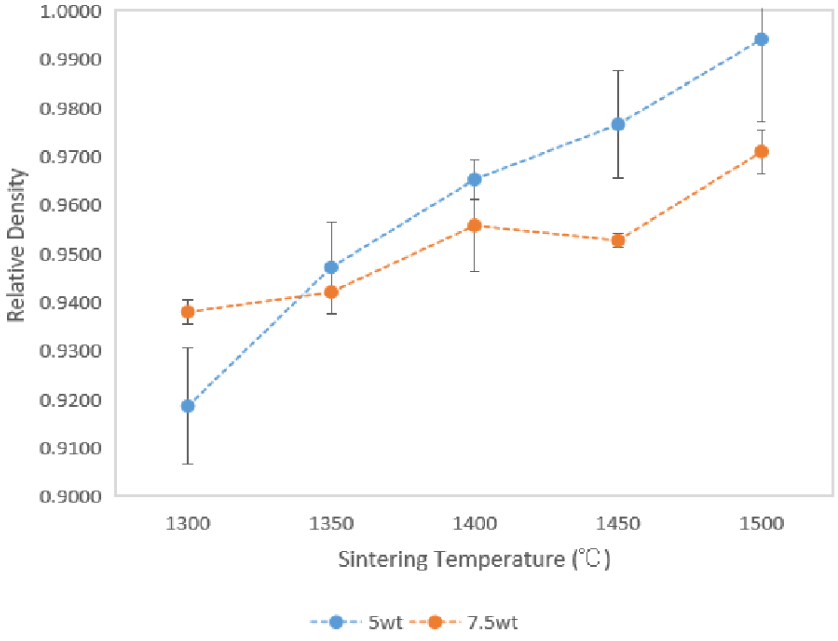

Figure 11: Relative density of Al_2O_3 - 5/7.5 wt% TiO_2 with respect to sintering temperature.

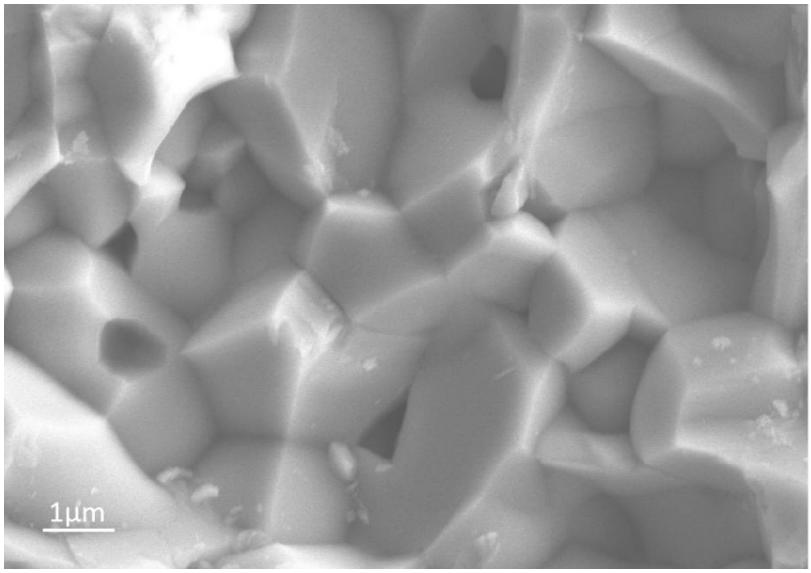

Figure 12: SEM-SE image of Al_2O_3-7.5wt%TiO_2 sintered at 1300℃ for 4hrs (fracture).

The addition of TiO_2 results in a notable reduction in the sintering temperature of Al_2O_3 compared to pure Al_2O_3. Given that the melting point of TiO_2 is approximately 1850℃, there is no liquid phase formation during the sintering process. Research indicates that TiO_2 significantly enhances crystal growth and the initial sintering of Al_2O_3. When Ti^{4+} ions substitute for Al^{3+} in the alumina lattice, they generate Al^{3+} vacancies due to charge imbalance[58, 59]. These vacancies play a crucial role in increasing the diffusion rates of ions within the crystal lattice, thereby facilitating faster sintering at lower temperatures. However, charge balance defects generated in this process impede the densification of ceramics.

4.1.2 Dielectric Properties

To ensure that the discussion of the results focuses on dense ceramic samples, all samples were sintered at temperatures above 1350℃. **Figure 13** and **Figure 14** present the permittivity and Qf of Al_2O_3 - TiO_2 samples sintered at various temperatures for 4 hours. The data indicate that permittivity increases with higher concentrations of TiO_2, while Qf decreases. This trend is consistent with the inherent properties of TiO_2, which exhibits a higher permittivity but a lower Qf compared to Al_2O_3. The permittivity values of 1375℃ sintered samples are lower than 1400℃ and 1450℃ sintered samples. This reveals that volume density is associated with permittivity [60].

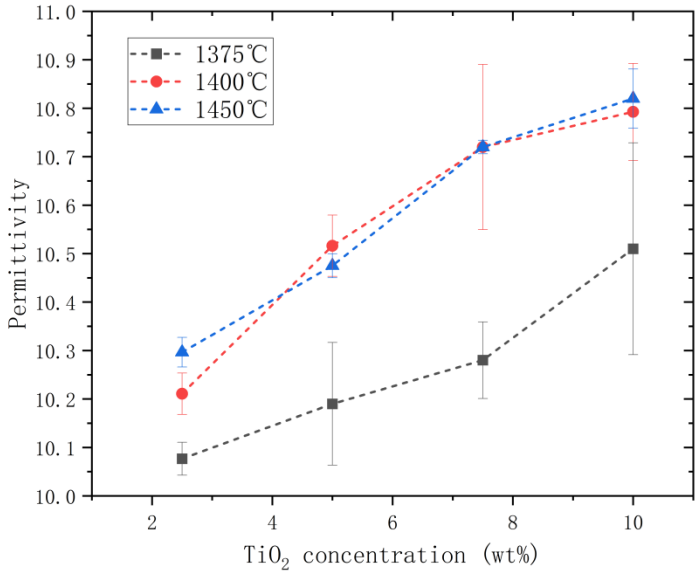

Figure 13: Permittivity of Al_2O_3 - 2.5/5/7.5/10 wt% TiO_2 with different sintering temperature.

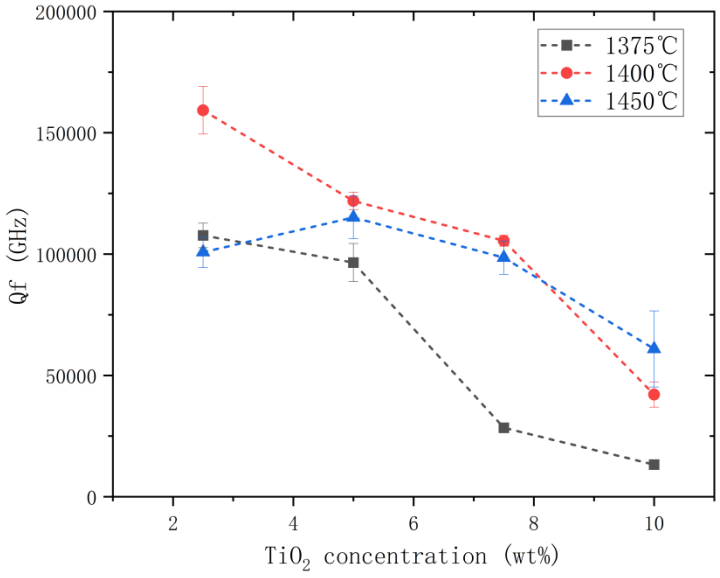

Figure 14: Qf of Al_2O_3 - 2.5/5/7.5/10 wt% TiO_2 with different sintering temperature.

From **Figure 15** and **Figure 16**, it is evident that the Qf is positively correlated with the duration of sintering. Longer sintering times generally facilitate more complete diffusion and grain growth, which leads to a reduction in the number of pores and other defects. This improvement in microstructural integrity enhances the Qf, as the material becomes more homogeneous and less susceptible to dielectric losses.

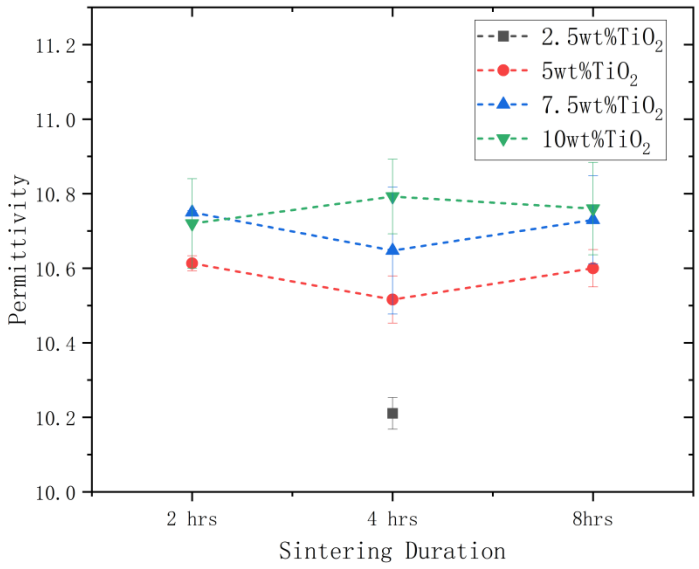

Figure 15: Permittivity of Al_2O_3 - 2.5/5/7.5/10 wt% TiO_2 with different sintering duration.

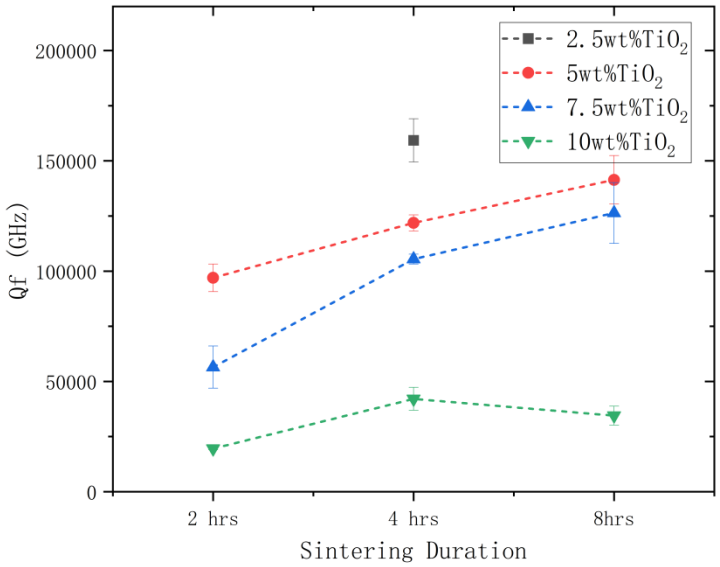

Figure 16: Qf of Al_2O_3 - 2.5/5/7.5/10 wt% TiO_2 with different sintering duration.

For all samples subjected to various heating processes, the changes in permittivity are minimal. This suggests that the dielectric constant remains relatively stable once the material attains a specific density and grain structure.

In summary, considering both permittivity and Qf, the optimal properties are achieved when the sintering temperature is approximately 1400℃, with low TiO_2 content and extended sintering duration.

According to the τ_f of Al_2O_3 and TiO_2, it's expected that τ_f will increase with the increase of TiO_2 content. However, in **Figure 17**, the increase in τ_f between Al_2O_3 samples with different TiO_2 contents is not as significant as anticipated, although some differences exist between samples with and without TiO_2. Even when the titania content was increased to 10 wt% τ_f it was still below -30 ppm/c, which was inconsistent with the calculated and reported data. Clearly, something happened in this system.

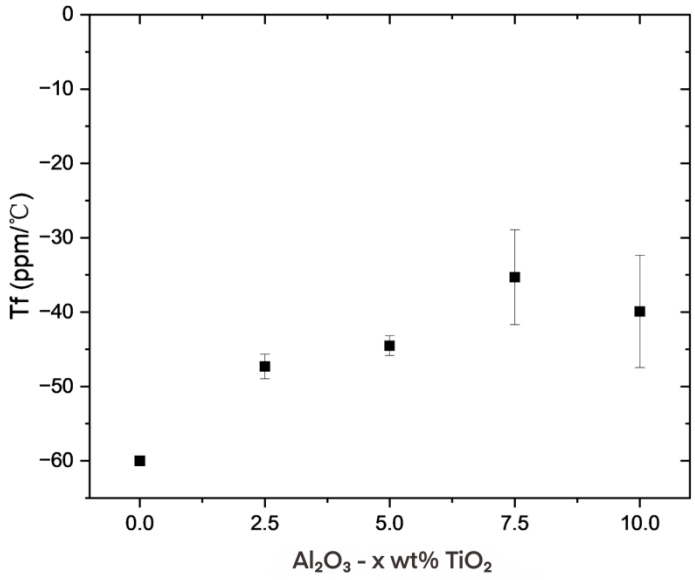

Figure 17: τ_f of Al_2O_3 – 0/2.5/5/7.5/10 wt% TiO_2 sintered at 1400℃ for 4 hrs.

4.1.3 Characterization

The most likely reason for the problem with τ_f is that the expected alumina-titanium oxide system did not form smoothly, and some other reaction occurred. **Figure 18** displays the XRD curves of Al_2O_3 ceramics with varying TiO_2 content.

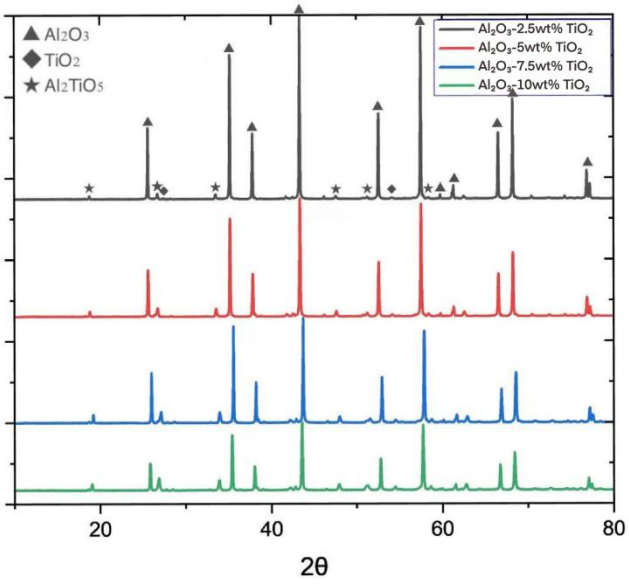

Figure 18: XRD curves of Al_2O_3 – 2.5/5/7.5/10 wt% TiO_2 sintered at 1400℃ for 4 hrs.

It is evident that a secondary phase, Al_2TiO_5, has formed. This could explain why the τ_f values of the samples do not align with expectations. The intensity of the characteristic peak of Al_2TiO_5 in the figure is proportional to the introduced titania content. It can be clearly found that Al_2O_3 with 2.5wt% TiO_2 sample has a lower Al_2TiO_5 characteristic peak than Al_2O_3 with 10wt%TiO_2 sample. At this time, the characteristic peak of titanium oxide is very small, which means that almost all titanium oxide has been converted into the second phase.

4.2 Annealing Treatment Effect

According to the phase diagram, the second phase will decompose at lower temperatures. Therefore, the sintered sample was annealed at 1000℃.

4.2.1 Dielectric Properties

As shown in **Figure 19** and **Figure 20**, the permittivity remains very stable with increasing annealing duration. Although Qf (quality factor) exhibits slight fluctuations, the overall changes are not significant.

Despite not being noticeable, the minor fluctuations in Qf suggest that the annealing process helps maintain the material's intrinsic quality factor by possibly reducing defects and optimizing

the grain structure. These slight variations could be attributed to minor changes in microstructure or residual stress relief during prolonged annealing.

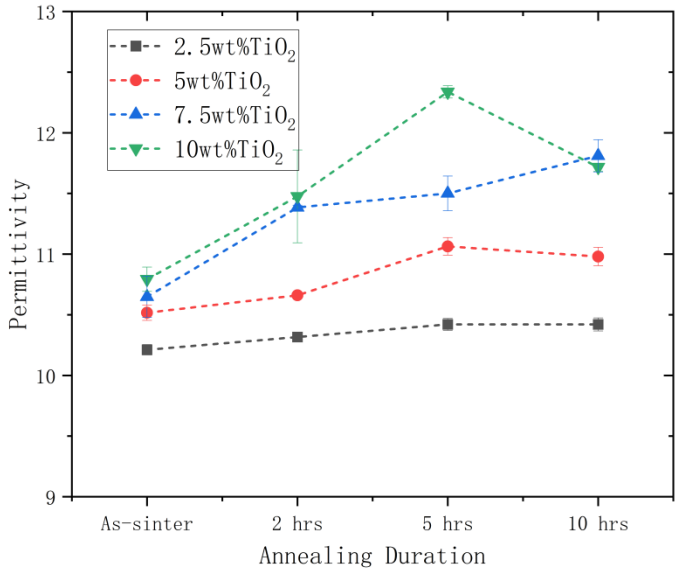

Figure 19: Permittivity of Al_2O_3 - 2.5/5/7.5/10 wt% TiO_2 with different annealing duration.

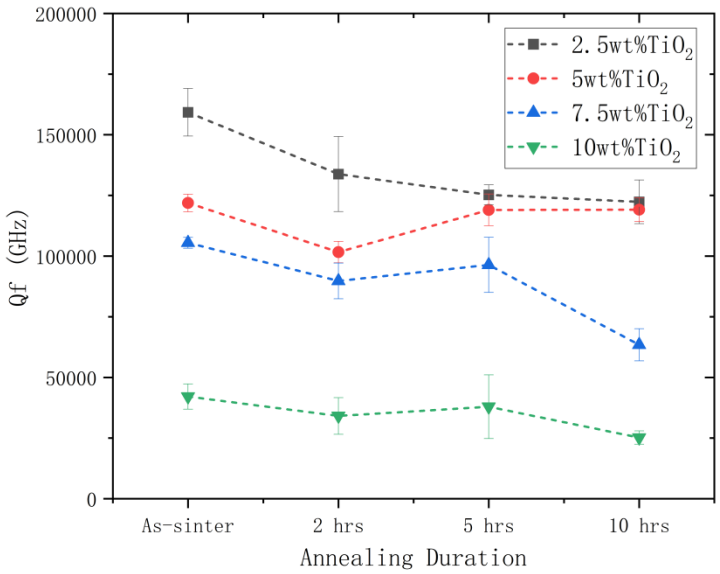

Figure 20: Qf of Al_2O_3 - 2.5/5/7.5/10 wt% TiO_2 with different annealing duration.

From **Figure 21**, it is clear that as the annealing duration increases, the property gradually increases until it reaches saturation after 5 hours.

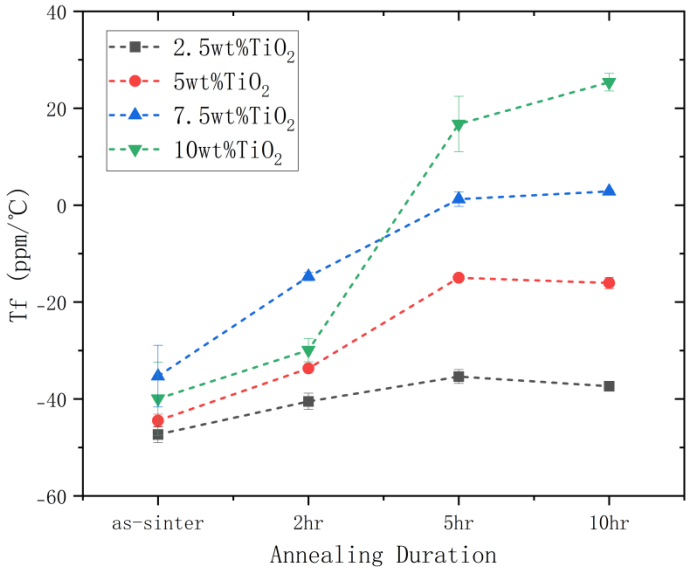

Figure 21: τ_f of Al_2O_3 - 2.5/5/7.5/10 wt% TiO_2 with different annealing duration.

Following the annealing process, The τ_f is found to be proportional to the TiO_2 content. Significantly, the property of Al_2O_3 with 7.5wt% TiO_2 can be improved to nearly zero. Specifically, after sintering at 1400°C for 4 hours and then annealing at 1000°C, τ_f of the Al_2O_3-7.5 wt% TiO_2 sample is measured at +1.25 ppm/°C.

This does not imply that τ_f can increase infinitely as the annealing time extends. As shown in **Figure 22**, after approximately five hours, it reaches saturation, τ_f become stable.

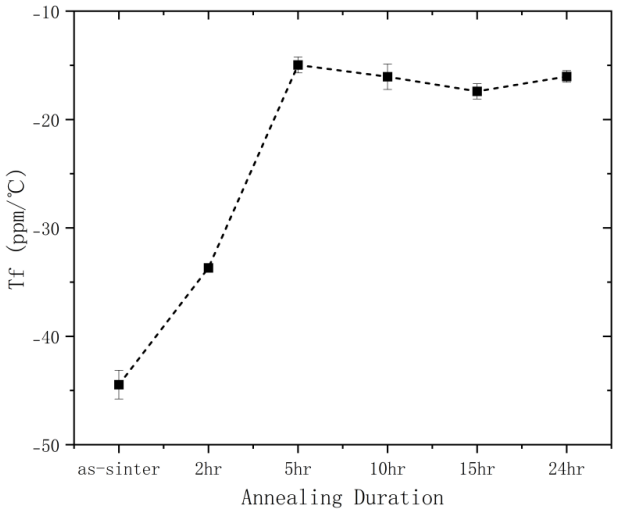

Figure 22: τ_f of Al_2O_3 - 5 wt% TiO_2 with 0/2 hrs/5 hrs/10 hrs/15 hrs/24 hrs annealing.

4.2.2 Characterization

DSC can be used to measure the decomposition temperature of the second phase. The DSC results of the sintered sample are presented in **Figure 23**. A distinct peak begins at 850℃, indicating that a phase reaction occurs at this temperature. The heat flow observed below 600°C is attributed to the evaporation of water from the sample. The exothermal reaction between 600°C and 800°C is caused by contamination combustion.

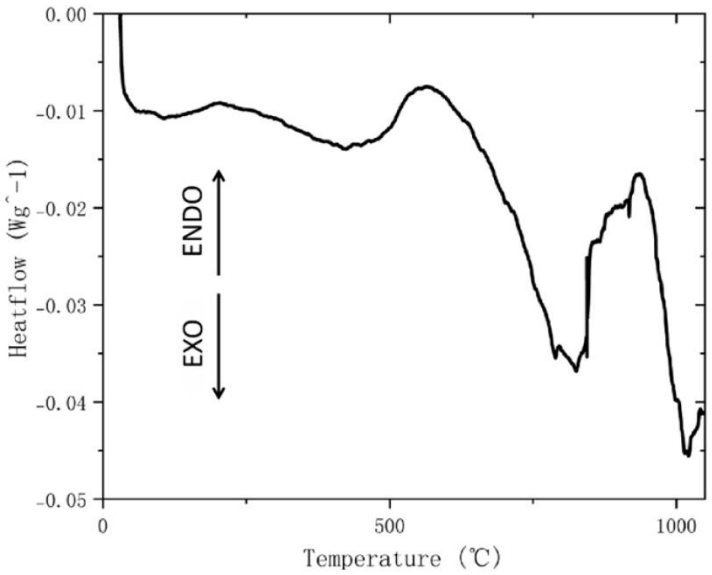

Figure 23: DSC of 1400℃ 4 hrs sintered Al_2O_3-7.5wt% TiO_2.

The XRD curves in **Figure 24** reveal that with increasing annealing time, the characteristic peaks of Al_2TiO_5 gradually disappear, which suggests that this phase is unstable at higher temperatures. After 5 hrs, the entire process of Al_2TiO_5 decomposition is almost finished at 1000. In this process, Al_2TiO_5 breaks down into Al_2O_3 and TiO_2.

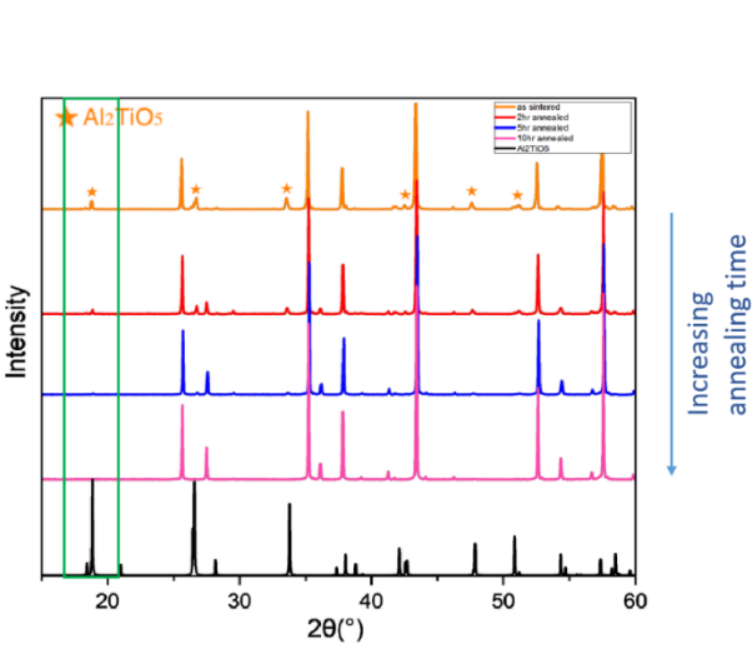

Figure 24: XRD curves of sintered Al_2O_3-7.5wt% TiO_2 sample with 1000℃ annealing temperature and different annealing time, the bottom is JCPDS of Al_2TiO_5.

Using SEM-BSE, phases with different atomic masses exhibit varying contrasts. Heavier atoms appear brighter in the image. In **Figure 25**, four distinct brightness levels can be observed: the darkest regions are pores, the dark gray region corresponds to Al_2O_3, the lightest to TiO_2, and the light gray regions to Al_2TiO_5. These differences in brightness indicate variations in the elemental composition of the grains.

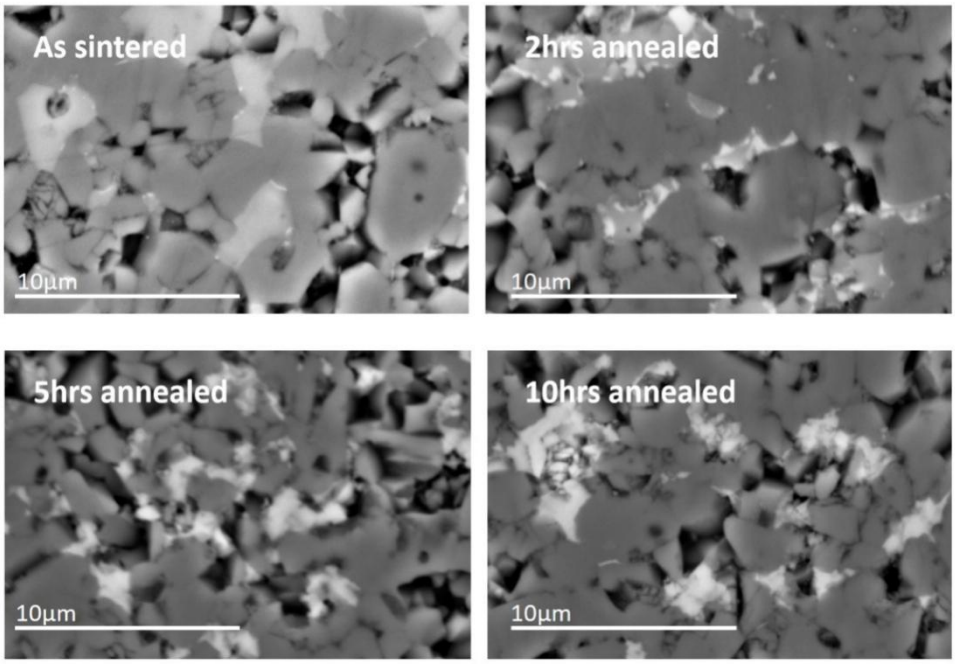

Figure 25: BSE images of sintered Al_2O_3-7.5wt% TiO_2 sample with different annealing duration.

In the sample without annealing, there only exit Al_2O_3 and Al_2TiO_5 two phases. After 2 hrs of annealing, there is a brighter contrast in the grain boundaries. Combined with previous XRD results, it can be inferred that this is the newly generated TiO_2. As the annealing duration increases, the proportion of Al_2TiO_5 decreases gradually, the newly formed TiO_2 takes the place originally occupied by Al_2TiO_5. After 10 hours of annealing, there almost only remain Al_2O_3 and TiO_2 phases. This characterizes the entire process of Al_2TiO_5 decomposition during the annealing process. The reduction in the Al_2TiO_5 phase with increased annealing time suggests the phase decomposition mechanism is driven by thermodynamic stability at elevated temperatures.

Figure 26, **Figure 27** and **Figure 28** illustrates the SEM-EDS images of the sintered samples subjected to varying annealing durations.

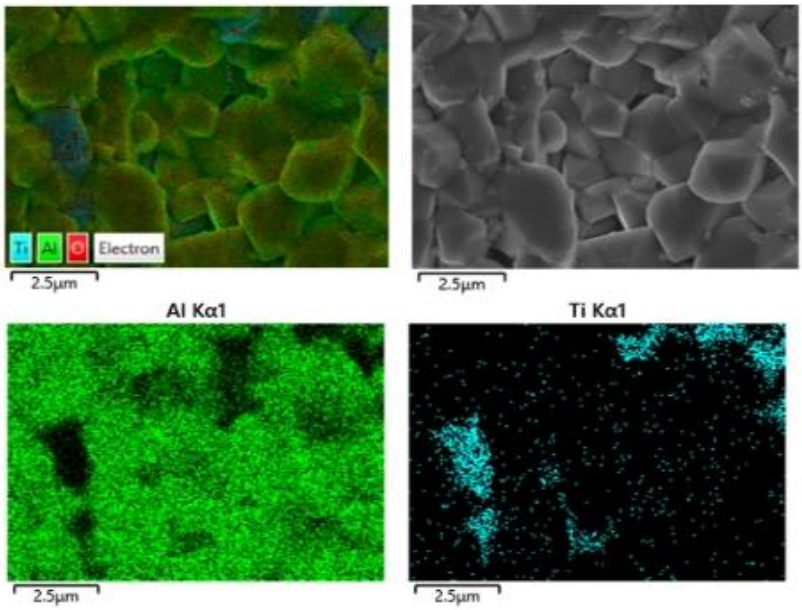

Figure 26: SEM-EDS images of as sintered Al_2O_3-7.5wt% TiO_2 sample.

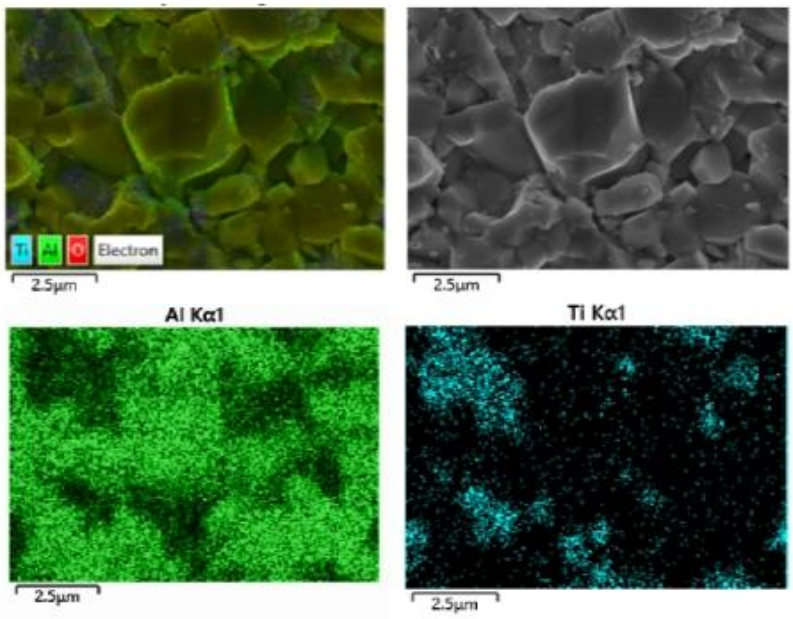

Figure 27: SEM-EDS images of the sintered Al_2O_3-7.5wt% TiO_2 sample annealed for 2 hrs.

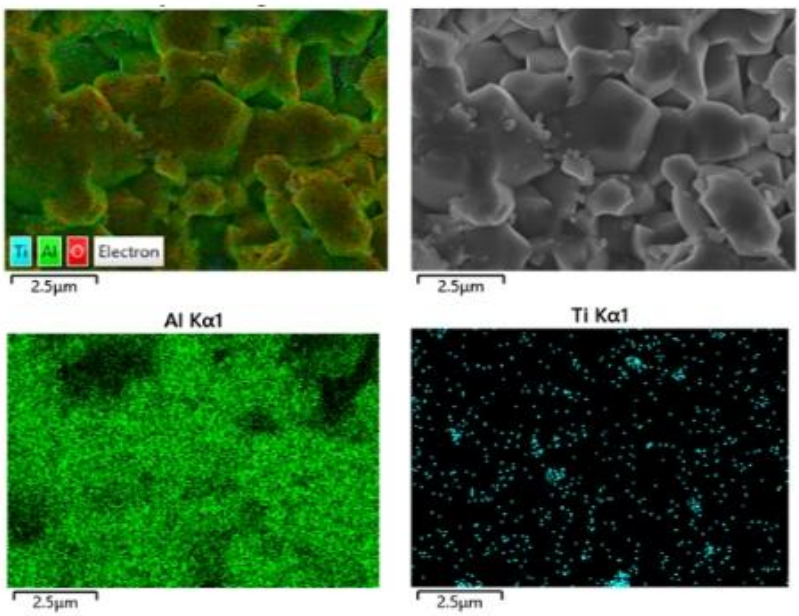

Figure 28: SEM-EDS images of the sintered Al_2O_3-7.5wt% TiO_2 sample annealed for 10 hrs.

The distribution of Al and Ti elements is more uniform in these samples, which significantly enhances the dielectric properties of the materials. This helps the dielectric properties of materials. This suggests that annealing plays a crucial role in homogenizing the elemental composition. This uniformity is essential for improving the dielectric properties because it reduces localized regions of differing electrical characteristics, which can lead to dielectric breakdown. Additionally, the enhanced dielectric properties can be attributed to the reduction

of defects and the improved densification through annealing. These changes contribute to a more stable dielectric response and potentially increase the material's suitability for dielectric applications.

4.3 Powder Processing Method Effect

Different methods of processing also affect the properties of ceramics. Here we compared three different ways to mix powders: High speed rotation by Thinky mixer, ball milling and slip casting. The Qf of materials proceeded by these methods are shown in **Figure 29**:

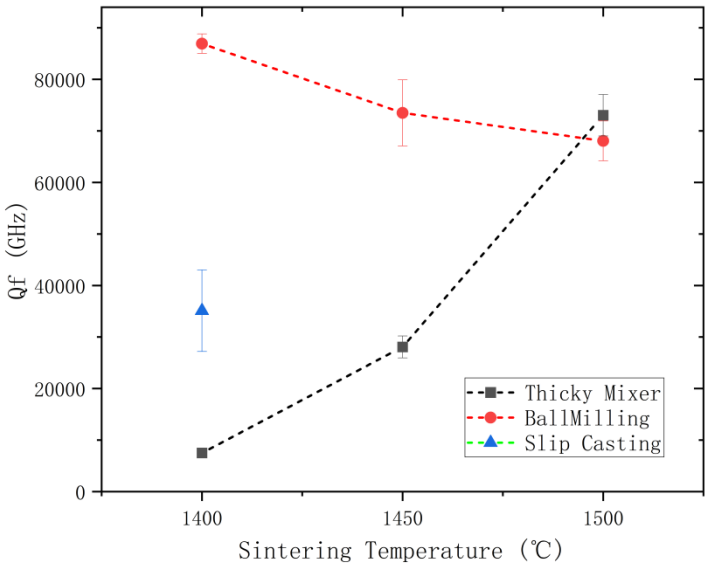

Figure 29: Qf of Al_2O_3(30nm, α+θ)-7.5wt% TiO_2 using different ways to processing raw powders.

Ball milling resulted in samples that were densified at lower sintering temperatures. As the sintering temperature increased, the Qf of the samples processed with a Thinky mixer gradually surpassed that of the ball-milled samples. Slip casting did not demonstrate a clear advantage over the other methods, suggesting that powder agglomeration doesn't affect this system much.

When using ball milling, selecting the appropriate milling duration is crucial. **Figure 30** shows the density and Qf values of samples subjected to different ball milling times. It is evident that as the ball milling time increases, the density of the samples also rises. However, the Qf value peaks after 8 hours of milling, having increased for a while, and then subsequently declines after 40 hours.

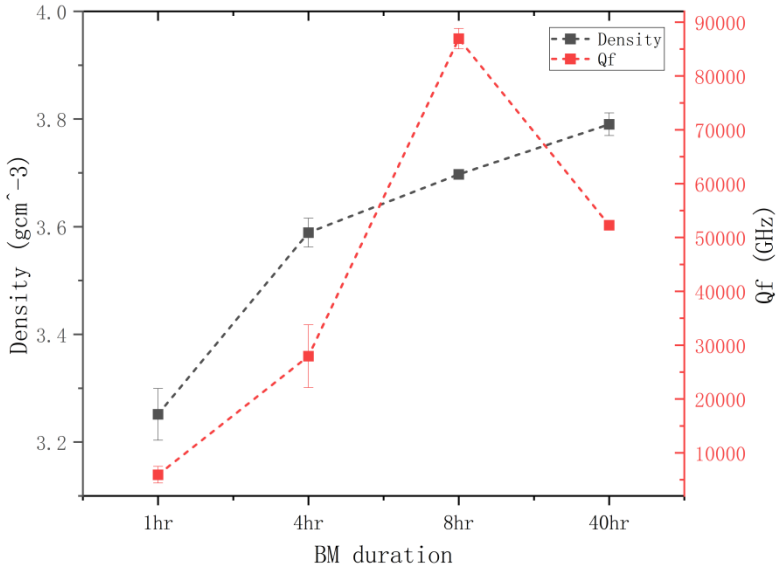

Figure 30: Density and Qf of Al_2O_3(30nm, α+θ)-7.5wt% TiO_2 with respect to ball milling duration. Samples were sintered at 1400℃ for 4 hrs.

The powder obtained by ball milling was tested by TGA, and the result curves are shown in **Figure 31**, which showed that as the ball milling time increased, the powder lost more weight during the sintering process. This means that more contamination exists in the powder, usually from the plastic bottle used in the ball mill. The plastic leaves carbon impurities in the ceramic sample after burning, affecting the dielectric properties of the sample.

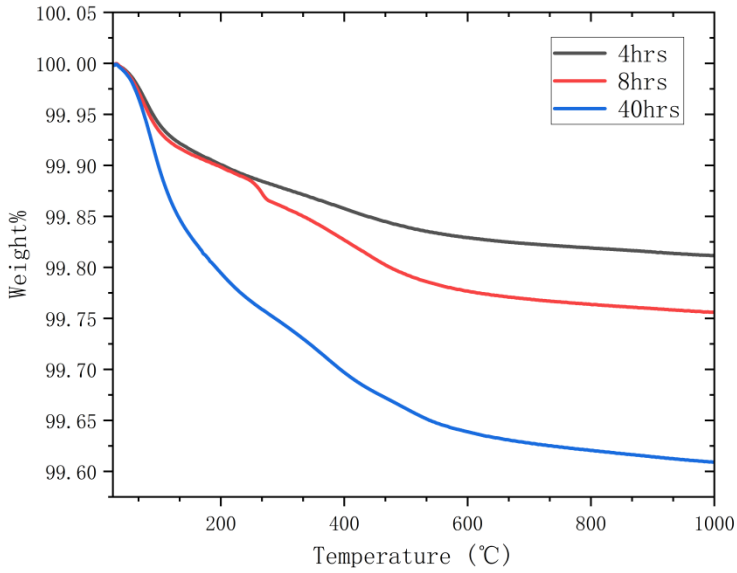

Figure 31: TGA curves of Al_2O_3(30nm, α+θ)-7.5wt% TiO_2 powder with different ball milling duration.

Short milling duration will cause bad density due to powder not being fully mixed; too long milling duration will introduce more contamination. Therefore, the ball milling time needs to be carefully selected.

4.4 Alumina Precursor Effect

4.4.1 Particle Size

Figure 32 and **Figure 33** show that both 30 nm and micron-sized alumina powders require significantly higher sintering temperatures. Even at the same density, the 150 nm sample exhibits superior dielectric loss properties. Comparing the 150 nm and micron-sized powders, both of which are α-Al_2O_3, the key difference lies in their grain size. In this context, the smaller grain size of the 150 nm powder aids in better sintering and improved properties. Smaller grains generally provide a higher surface area, which can enhance diffusion during sintering, leading to improved densification and better dielectric properties.

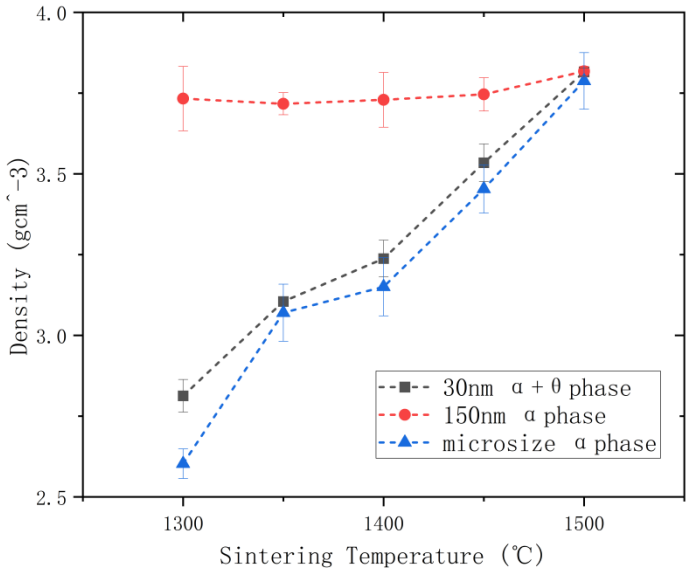

Figure 32: Density of sintered Al_2O_3-7.5wt% TiO_2 sample with different Al_2O_3 particle size and sintering temperature.

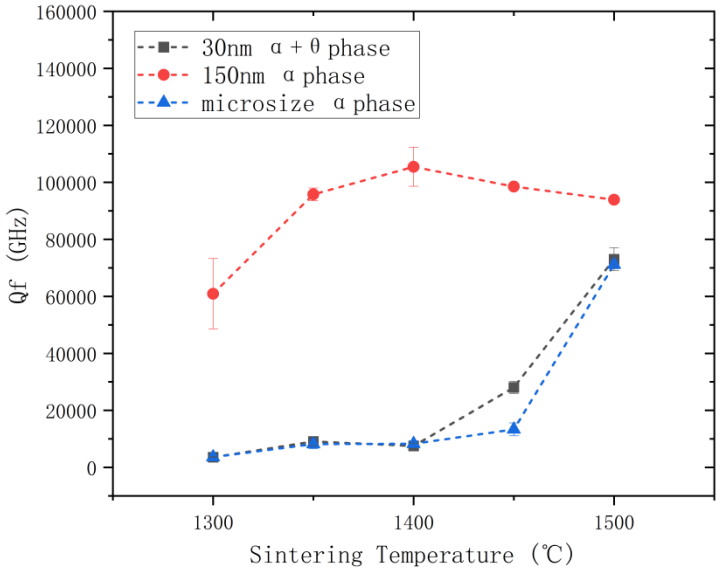

Figure 33: Qf of sintered Al_2O_3-7.5wt% TiO_2 sample with different Al_2O_3 particle size and sintering temperature.

However, the results for the 30 nm powder do not support this trend, likely due to several factors: 1)the presence of θ-phase alumina, θ-phase alumina has different crystallographic and dielectric characteristics, which could degrade the overall performance. 2) a wider particle size distribution (PSD), A broad PSD can lead to non-uniform densification during sintering. Smaller particles sinter at different rates compared to larger particles, potentially resulting in an inhomogeneous microstructure and suboptimal dielectric properties. 3) aggregation issues, Nano-sized powders tend to aggregate due to their high surface energy. These aggregates can act as defects during sintering, impeding densification and leading to a less uniform microstructure. This can negatively impact the dielectric properties. All these factors may influence the final result.

4.4.2 Particle Size Distribution

Even with similar grain sizes, their particle distribution could be different. As shown in **Figure 34**, both 30 nm and micron-size alumina result in lower density and Qf, as previously discussed. Among the other powders, the 150 nm and 400 nm powders are commercial products, while the 150 nm-1200 powder is the 150 nm powder subjected to heat treatment at 1200°C for 30 minutes. According to DLS measurements, the d50 for this heat-treated powder is 444 nm. The

400 nm alumina sample has a particle size and sintered density similar to the 444 nm sample, yet there is a significant disparity in their Qf values.

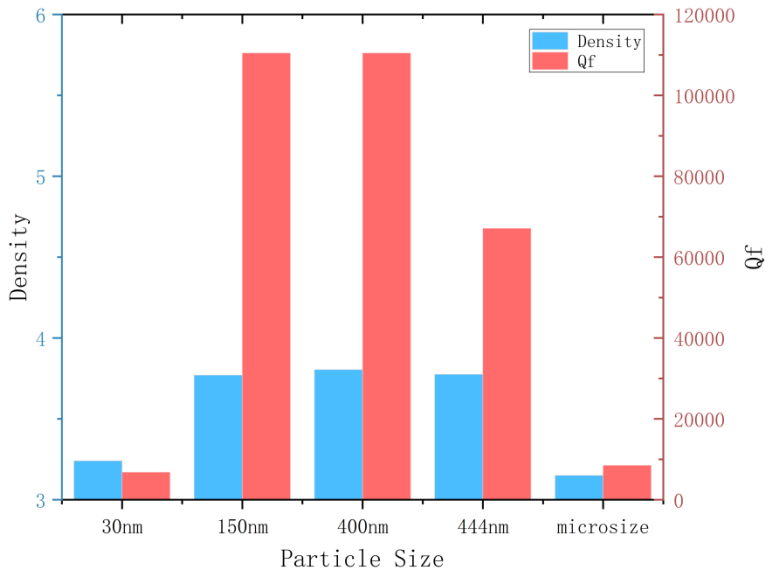

Figure 34: Density and Qf of Al_2O_3-7.5wt% TiO_2 sample with different Al_2O_3 particle sizes which are sintered at 1400°C for 4hrs. 444nm alumina is obtained using 150nm alumina heat treated at 1200°C for 30min. The rest powders are commercial.

Figure 35 presents the particle size distribution graphs for different alumina powders. It is observed that the commercial 400 nm powder exhibits a good normal distribution, whereas the heat-treated powder shows a bimodal distribution. This uneven distribution in the 150 nm-1200 powder caused by heat treatment likely results in non-uniform grain growth and distribution during sintering. This non-uniformity can hinder the effective packing and densification required for optimal dielectric properties. The presence of larger particles amidst a predominantly finer matrix can disrupt the continuity of the microstructure, increasing the likelihood of porosity and reducing the Qf.

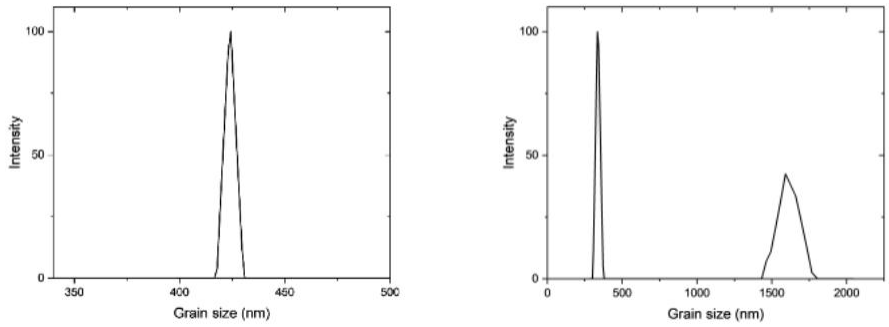

Figure 35: Left: particle size distribution of 400nm powder. Right: particle size distribution of 1500nm-1200(d50=444nm) powder.

Besides grain size distribution, the heat treatment at 1200°C might have led to a different microstructure in the 150 nm-1200 powder compared to the commercial 400 nm powder. Factors such as grain boundary characteristics, the presence of residual stresses, and the homogeneity of the sintered material can also impact Qf. Heat treatment processes can introduce impurities or defects that degrade Qf. These could be absent or less pronounced in the commercially prepared 400 nm powder

4.4.3 Phases

Alumina has many phases; in addition to the most common α phase, γ phase, and θ phase alumina precursors were selected for comparison. The XRD curves of these alumina powders are shown in **Figure 36**.

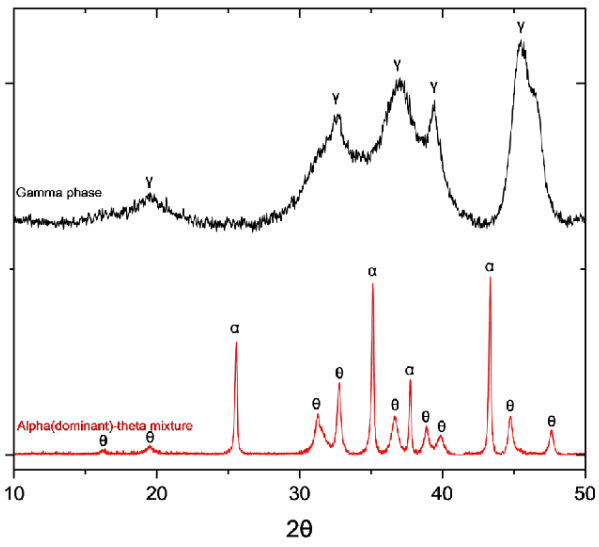

Figure 36: XRD pattern of different alumina powders.

Figure 37 presents Qf for sintered samples using different alumina phase precursors. From the data, it is evident that α-alumina precursors lead to the best Qf results. γ-alumina precursors show peak properties at 1450°C, with a decline in properties as the temperature increases. The α-θ mixed alumina precursors require the highest temperature to achieve complete sintering. These variations highlight the significant impact of precursor phases on the sintering process and the properties of the ceramics.

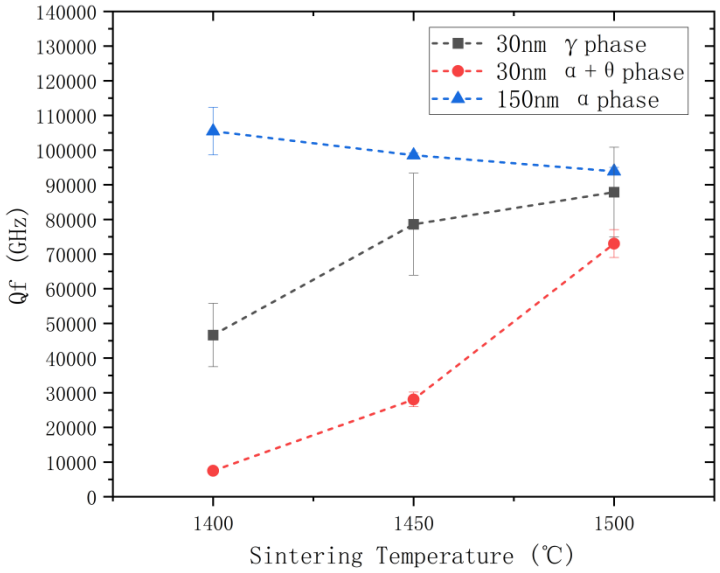

Figure 37: Qf of Al_2O_3-7.5wt% TiO_2 with different alumina phases.

After sintering, nano alumina turns into a stable α phase, but the phase conversion process during sintering can adversely affect densification and properties. Single-phase alumina precursor is preferred at lower sintering temperatures.

4.5 Other Dopant Effect

4.5.1 Al_2O_3-TiO_2-Nb_2O_5/ Mn_2O_3-$BaZrO_3$-ZnO

Adding different dopants can help alumina-titania ceramics sinter and improve the properties of the ceramics. Here, we designed two formulas: 93.5wt% Al_2O_3-6.5wt% TiO_2-0.3wt% Nb_2O_5-0.5wt% $BaZrO_3$-0.25/0.5/0.75wt% ZnO and 93.5wt% Al_2O_3-6.5wt% TiO_2-0.3wt% Nb_2O_5-0.08wt% Mn_2O_3-0.5wt% $BaZrO_3$-0.25/0.5/0.75wt% ZnO. Al_2O_3-TiO_2 ceramics doped with Nb_2O_5 exhibit higher compressive strength and abrasion resistance compared to pure

alumina ceramics. This improvement is attributed to enhanced grain boundary diffusion and increased strain energy from Nb^{5+} cation substitution. Nb_2O_5 serves as an effective additive for lowering sintering temperatures in Al_2O_3-based ceramics [61]. The dielectric properties of Al_2O_3-TiO_2 can be improved by addition of ZnO [62].

The Qf of samples are shown in **Figure 38**:

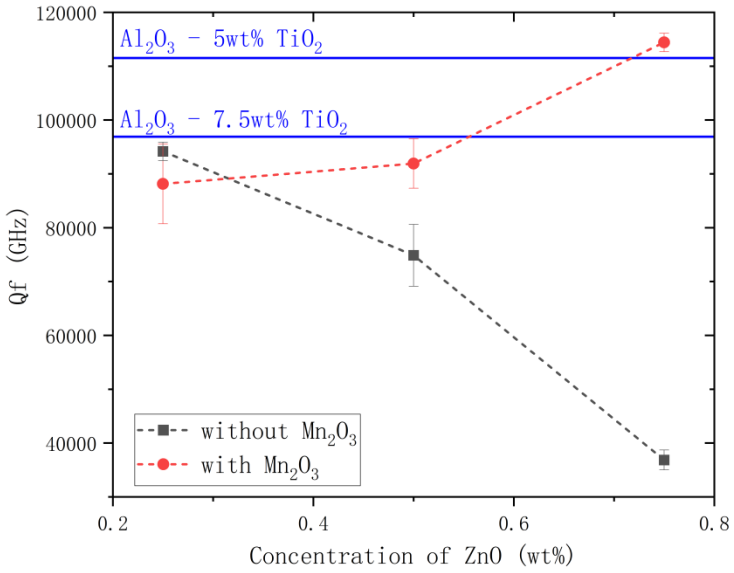

Figure 38: Qf of 93.5wt% Al_2O_3-6.5wt% TiO_2-0.3wt% Nb_2O_5-0.5wt% $BaZrO_3$-0.25/0.5/0.75wt% ZnO (Without Mn_2O_3) and 93.5wt% Al_2O_3-6.5wt% TiO_2-0.3wt% Nb_2O_5-0.08wt% Mn_2O_3-0.5wt% $BaZrO_3$-0.25/0.5/0.75wt% ZnO (With Mn_2O_3) samples.

Without Mn_2O_3, the Qf is negatively correlated with ZnO concentration while with Mn_2O_3 samples shows the inverse tendency. For 93.5wt% Al_2O_3-6.5wt% TiO_2-0.3wt% Nb_2O_5-0.08wt% Mn_2O_3-0.5wt% $BaZrO_3$-0.25/0.5/0.75wt% ZnO sample, the Qf is even higher than Al_2O_3-5wt% TiO_2 in same sintering conditions, this means that this material has great potential in microwave dielectric applications.

4.5.2 Bi_2O_3 Dopant

Bismuth oxide has a melting point of 824°C, which is lower than the sintering temperature of alumina. We intend to introduce a small amount of bismuth oxide to create a liquid phase during the sintering process that will facilitate sintering and lower the overall temperature required.

At 1300°C, the second phase Al_2TiO_5 does not form. This means that we can avoid the subsequent annealing process by lowering the sintering temperature. Therefore, using dopant to reduce sintering temperature is an attractive approach. The Qf of Bi_2O_3 doped samples are shown in **Figure 39**:

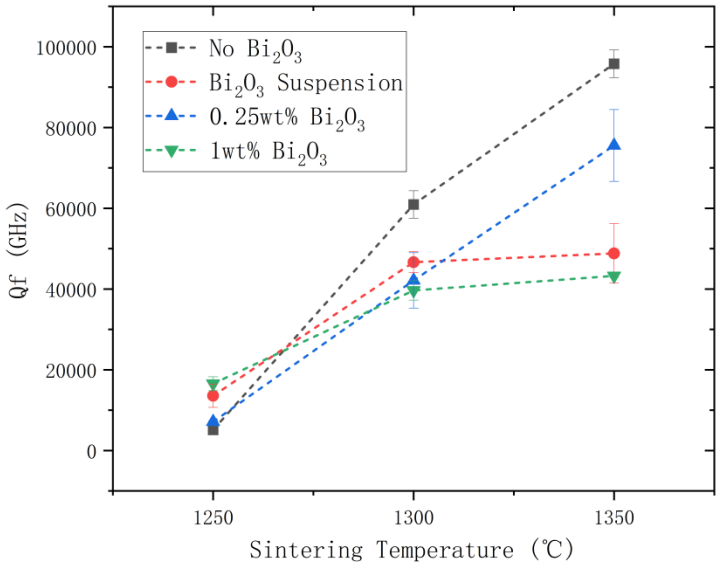

Figure 39: Qf of Al_2O_3-7.5wt% TiO_2 adding Bi_2O_3 dopants.

At lower temperatures (1250°C), Bi_2O_3 dopant increases the sintering degree of the sample, but as the temperature increases, its negative impact on Qf far outweighs its advantages. Therefore, Bi_2O_3 is not suitable for this system.

4.5.3 MgO Dopant

MgO can effectively enhance densification and develop more uniform microstructures [63, 64]. The accepted mechanism by which Mg enhances densification is increased surface diffusion of pores, which enables them to move at the same velocity as grain boundaries (whose mobility is lowered by Mg solute-drag).[65] Table 3 shows the density and Qf of Al_2O_3-7.5wt% TiO_2 with MgO dopants.

Table 3: Density and Qf of Al_2O_3-7.5wt% TiO_2 with MgO dopants sintered at 1400℃ for 4 hrs.

Sample	Relative density	Qf (GHz)
No dopants	0.96	101992
1 wt% $Mg(NO_3)_2 \cdot 6H_2O$	0.93	15866
2 wt% $Mg(NO_3)_2 \cdot 6H_2O$	0.91	26345

After adding the dopant, the density of the sample is even lower than that of the sample without the dopant, suggesting that MgO affects the sintering temperature, requiring a longer time or higher temperature for complete sintering.

2 wt% $Mg(NO_3)_2 \cdot 6H_2O$ sample has a lower density compared to a 1 wt% $Mg(NO_3)_2 \cdot 6H_2O$ sample, yet it exhibits a higher Qf value. This indicates that factors other than density influence Qf. It's suggested that while the density of the sample increases, the particle size decreases, resulting in more grain boundaries, which can adversely affect Qf.

4.6 Dielectric Properties at 10 GHz

Figure 40 shows the permittivity of Al_2O_3 – 2.5/5/7.5/10 wt% TiO_2 measured by SPDR at 10GHz. The permittivity does not show a clear trend with temperature, which may be related to the defects in the large sample. It can be seen that the higher the titanium oxide content in the sample, the larger the permittivity. Compared with the results measured by the Hakki–Coleman method, the permittivity measured by SPDR is generally lower.

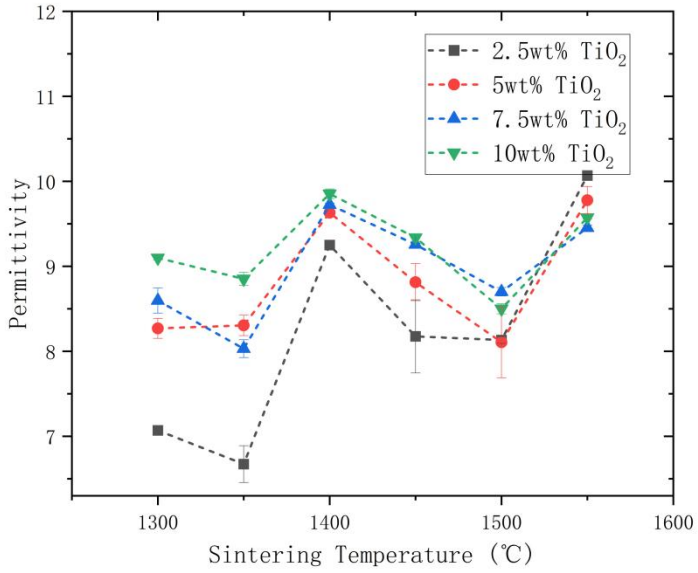

Figure 40: Permittivity of Al_2O_3 – 2.5/5/7.5/10 wt% TiO_2 measured by SPDR at 10GHz

The dielectric loss of Al_2O_3 – 2.5/5/7.5/10 wt% TiO_2 measured by SPDR at 10GHz is shown in **Figure 41** As the sintering temperature increases, the dielectric loss decreases rapidly, reaching 10^{-5} levels at around 1500 ℃. Al_2O_3 – 2.5 wt% TiO_2 sintered at 1500℃ obtain the lowest dielectric loss ($\tan\delta = 2x10^{-5}$).

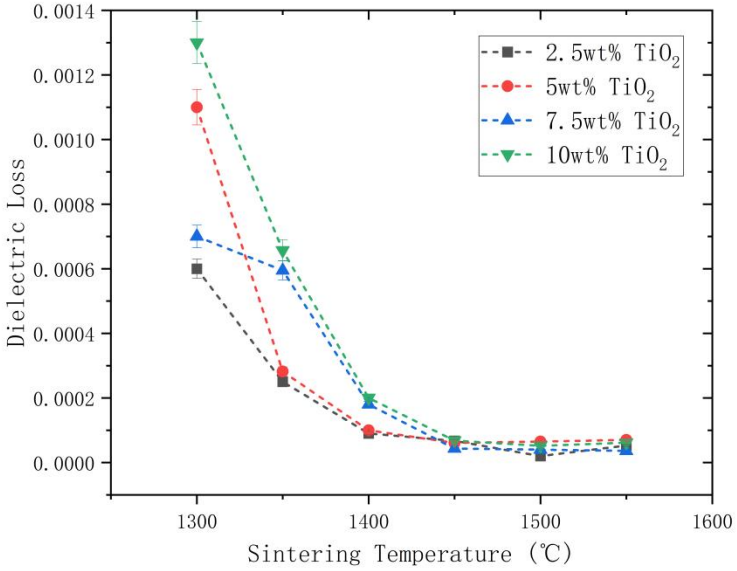

Figure 41: Dielectric loss of Al_2O_3 – 2.5/5/7.5/10 wt% TiO_2 measured by SPDR at 10GHz

Typical uncertainty of the real permittivity is better than ±1%, providing that the thickness of a sample under test is measured with accuracy ±0.7% or better. The dielectric loss uncertainty is

±5 percent, and the dielectric loss resolution is 2 x 105. These uncertainties can be caused by a systematic error associated with uncertainties in thickness and dielectric permittivity of the dielectric resonator. With decreasing values of dielectric loss and permittivity, the uncertainties increase [9, 29].

It is reported that the permittivity of pure alumina is 9.42±0.3%, and dielectric loss is 2.4×10^{5} $\pm 2 \times 10^{5}$ using SPDR at 3.9 GHz [9]. Our dielectric loss results are consistent with the reported data, and some permittivity results are lower than reported data.

5. Summary and Conclusions

In this research, excellent dielectric properties εr = 10.73, Qf = 126,347 GHz were obtained by sintering submicron Al_2O_3 with 7.5 wt% TiO_2 at 1400ºC for 8 hours. After annealing at 1000°C for 5 hrs, the τ_f reaches at +1.25 ppm/°C which is very close to zero.

TiO_2 helps the sintering of Al_2O_3 by vacancy mechanism and phase reaction. The sintering temperature of Al_2O_3 lower 100-200°C by adding TiO_2. However, increasing TiO_2 content introduces a critical trade-off: while εr and τf improve, Qf degrades. The persistent negative τf at high TiO_2 concentrations is attributed to secondary Al_2TiO_5 phase formation above 1280°C. Low-temperature annealing effectively decomposes Al_2TiO_5, redistributes Ti uniformly, and balance τ_f to near-zero.

Ball milling optimizes mixing but requires strict time control to avoid contamination-induced Qf loss. Submicron Al_2O_3 with narrow particle size distribution and pure phase composition minimizes sintering defects, achieving high relative density at lower sintering temperature. 93.5wt% Al_2O_3-6.5wt% TiO_2-0.3wt% Nb_2O_5-0.08wt% Mn_2O_3-0.5wt% $BaZrO_3$-0.75wt% ZnO has higher Qf compared with binary systems of Al_2O_3-TiO_2.

6. Future Work

It is clear that the addition of titanium oxide significantly lowers the sintering temperature of aluminum oxide. Studies indicate that both Ti^{3+} and Ti^{4+} are present in air-fired samples of the solid solution of TiO_2 in Al_2O_3, whereas only Ti^{3+} is found in hydrogen-fired samples [66]. This raises an interesting to investigate the relationship between the chemical valence state of Ti and the sintering behavior of ceramics. X-ray photoelectron spectroscopy (XPS) will be used to confirm the existence of titanium and analyze the ratio of Ti with different valences. Additionally, exploring the distribution of titanium oxide within aluminum oxide is also crucial for understanding the mechanisms of solid-state reaction between Al_2O_3 and TiO_2.

For 93.5wt% Al_2O_3-6.5wt% TiO_2-0.3wt% Nb_2O_5-0.5wt% $BaZrO_3$-0.25/0.5/0.75wt% ZnO samples, Qf decrease with the increasing of ZnO concentration, but for 93.5wt% Al_2O_3-6.5wt% TiO_2-0.3wt% Nb_2O_5-0.08wt% Mn_2O_3-0.5wt% $BaZrO_3$-0.25/0.5/0.75wt% ZnO (With Mn_2O_3) samples, Qf increase with the increasing of ZnO concentration. The reason behind adding such a small amount of Mn_2O_3 causes a different tendency and is worth discovering.

It is reported that MgO solutes can increase the densification rate [67] due to lowering the grain boundary mobility in Al_2O_3 [61, 62]. However, in my results, alumina with MgO dopant shows lower density and worse properties. The reasons for this result need to be ascertained.

7. References

[1] A. J. Moulson and J. M. Herbert, *Electroceramics*. Wiley, 2003. doi: 10.1002/0470867965.

[2] R. D. Richtmyer, "Dielectric Resonators," *J Appl Phys*, vol. 10, no. 6, pp. 391–398, Jun. 1939, doi: 10.1063/1.1707320.

[3] Sebastian M. T., *Dielectric materials for wireless communication*. 2008.

[4] H. Yang *et al.*, "The latest process and challenges of microwave dielectric ceramics based on pseudo phase diagrams," *Journal of Advanced Ceramics*, vol. 10, no. 5, pp. 885–932, Oct. 2021, doi: 10.1007/s40145-021-0528-4.

[5] H. Ohsato, T. Tsunooka, T. Sugiyama, K. Kakimoto, and H. Ogawa, "Forsterite ceramics for millimeterwave dielectrics," *J Electroceram*, vol. 17, no. 2–4, pp. 445–450, Dec. 2006, doi: 10.1007/s10832-006-0452-6.

[6] I. M. Reaney and D. Iddles, "Microwave Dielectric Ceramics for Resonators and Filters in Mobile Phone Networks," *Journal of the American Ceramic Society*, vol. 89, no. 7, pp. 2063–2072, Jul. 2006, doi: 10.1111/j.1551-2916.2006.01025.x.

[7] P. Guillon and Y. Garault, "Accurate Resonant Frequencies of Dielectric Resonators," *IEEE Trans Microw Theory Tech*, vol. 25, no. 11, pp. 916–922, Nov. 1977, doi: 10.1109/TMTT.1977.1129241.

[8] R. S. Kwok and Ji-Fuh Liang, "Characterization of high-Q resonators for microwave filter applications," *IEEE Trans Microw Theory Tech*, vol. 47, no. 1, pp. 111–114, 1999, doi: 10.1109/22.740093.

[9] J. Krupka, A. P. Gregory, O. C. Rochard, R. N. Clarke, B. Riddle, and J. Baker-Jarvis, "Uncertainty of complex permittivity measurements by split-post dielectric resonator technique," *J Eur Ceram Soc*, vol. 21, no. 15, pp. 2673–2676, Jan. 2001, doi: 10.1016/S0955-2219(01)00343-0.

[10] J. Sheen, "Study of microwave dielectric properties measurements by various resonance techniques," *Measurement*, vol. 37, no. 2, pp. 123–130, Mar. 2005, doi: 10.1016/j.measurement.2004.11.006.

[11] A. Templeton, X. Wang, S. J. Penn, S. J. Webb, L. F. Cohen, and N. McN. Alford, "Microwave Dielectric Loss of Titanium Oxide," *Journal of the American Ceramic Society*, vol. 83, no. 1, pp. 95–100, Jan. 2000, doi: 10.1111/j.1151-2916.2000.tb01154.x.

[12] S. KAWASHIMA, M. NISHIDA, I. UEDA, and H. OUCHI⋆, "Ba(Zn $_{1/3}$ Ta $_{2/3}$)O $_{3}$ Ceramics with Low Dielectric Loss at Microwave Frequencies," *Journal of the American Ceramic Society*, vol. 66, no. 6, pp. 421–423, Jun. 1983, doi: 10.1111/j.1151-2916.1983.tb10074.x.

[13] D. J. BARBER, K. M. MOULDING, J. ZHOU, and M. LI, "Structural order in $Ba(Zn_{1/3}Ta_{2/3})O_3$, $Ba(Zn_{1/3}Nb_{2/3})O_3$ and $Ba(Mg_{1/3}Ta_{2/3})O_3$ microwave dielectric ceramics," *J Mater Sci*, vol. 32, no. 6, pp. 1531–1544, 1997, doi: 10.1023/A:1018574505601.

[14] M. Onoda, J. Kuwata, K. Kaneta, K. Toyama, and S. Nomura, "$Ba(Zn_{1/3}Nb_{2/3})O_3$–$Sr(Zn_{1/3}Nb_{2/3})O_3$ Solid Solution Ceramics with Temperature-Stable High Dielectric Constant and Low Microwave Loss," *Jpn J Appl Phys*, vol. 21, no. 12R, p. 1707, Dec. 1982, doi: 10.1143/JJAP.21.1707.

[15] D. A. Sagala and S. Nambu, "Microscopic Calculation of Dielectric Loss at Microwave Frequencies for Complex Perovskite $Ba(Zn_{1/3}Ta_{2/3})O_3$," *Journal of the American Ceramic Society*, vol. 75, no. 9, pp. 2573–2575, Sep. 1992, doi: 10.1111/j.1151-2916.1992.tb05613.x.

[16] P. J. Harrop, "Temperature coefficients of capacitance of solids," *J Mater Sci*, vol. 4, no. 4, pp. 370–374, Apr. 1969, doi: 10.1007/BF00550407.

[17] E. L. Colla, I. M. Reaney, and N. Setter, "Effect of structural changes in complex perovskites on the temperature coefficient of the relative permittivity," *J Appl Phys*, vol. 74, no. 5, pp. 3414–3425, Sep. 1993, doi: 10.1063/1.354569.

[18] I. M. Reaney, E. L. C. Enrico L. Colla, and N. S. Nava Setter, "Dielectric and Structural Characteristics of Ba- and Sr-based Complex Perovskites as a Function of Tolerance Factor," *Jpn J Appl Phys*, vol. 33, no. 7R, p. 3984, Jul. 1994, doi: 10.1143/JJAP.33.3984.

[19] R. N. Clarke *et al.*, "A guide to the characterisation of dielectric materials at RF and microwave frequencies.," 2003. [Online]. Available: https://api.semanticscholar.org/CorpusID:189989258

[20] R. G. Geyer *et al.*, "Measuring the permittivity and permeability of lossy materials : solids, liquids, metals, building materials, and negative-index materials," 2005. [Online]. Available: https://api.semanticscholar.org/CorpusID:139882682

[21] J. Krupka, "Frequency domain complex permittivity measurements at microwave frequencies," *Meas Sci Technol*, vol. 17, no. 6, pp. R55–R70, Jun. 2006, doi: 10.1088/0957-0233/17/6/R01.

[22] L. F. Chen, C. K. Ong, C. P. Neo, V. V. Varadan, and V. K. Varadan, *Microwave Electronics*. Wiley, 2004. doi: 10.1002/0470020466.

[23] M. Sucher and J. Fox, *Handbook_of_Microwave_Measurements*. New York: Brooklyn Polytechnic Press, 1963.

[24] Y. Kobayashi and M. Katoh, "Microwave Measurement of Dielectric Properties of Low-Loss Materials by the Dielectric Rod Resonator Method," *IEEE Trans Microw Theory Tech*, vol. 33, no. 7, pp. 586–592, Jul. 1985, doi: 10.1109/TMTT.1985.1133033.

[25] X. Deming and Li Zhaonian, "A Novel Method for Characterizing the Surface Resistance of Two Conducting Plates Shorted at Both Ends of a Dielectric Resonator," in *15th European*

Microwave Conference, 1985, IEEE, Oct. 1985, pp. 912–916. doi: 10.1109/EUMA.1985.333594.

[26] B. W. Hakki and P. D. Coleman, "A Dielectric Resonator Method of Measuring Inductive Capacities in the Millimeter Range," *IEEE Trans Microw Theory Tech*, vol. 8, no. 4, pp. 402–410, Jul. 1960, doi: 10.1109/TMTT.1960.1124749.

[27] W. E. Courtney, "Analysis and Evaluation of a Method of Measuring the Complex Permittivity and Permeability Microwave Insulators," *IEEE Trans Microw Theory Tech*, vol. 18, no. 8, pp. 476–485, Aug. 1970, doi: 10.1109/TMTT.1970.1127271.

[28] J. Krupka, "Measurements of the complex permittivity of microwave circuit board substrates using split dielectric resonator and reentrant cavity techniques," in *Seventh International Conference on Dielectric Materials, Measurements and Applications*, IEE, 1996, pp. 21–24. doi: 10.1049/cp:19960982.

[29] J. Mazierska, J. Krupka, M. V. Jacob, and D. Ledenyov, "Complex permittivity measurements at variable temperatures of low loss dielectric substrates employing split post and single post dielectric resonators," in *2004 IEEE MTT-S International Microwave Symposium Digest (IEEE Cat. No.04CH37535)*, IEEE, 2004, pp. 1825–1828. doi: 10.1109/MWSYM.2004.1338959.

[30] J. Krupka, S. A. Gabelich, K. Derzakowski, and B. M. Pierce, "Comparison of split post dielectric resonator and ferrite disc resonator techniques for microwave permittivity measurements of polycrystalline yttrium iron garnet," *Meas Sci Technol*, vol. 10, no. 11, pp. 1004–1008, Nov. 1999, doi: 10.1088/0957-0233/10/11/305.

[31] E. J. Vanzura, J. R. Baker-Jarvis, J. H. Grosvenor, and M. D. Janezic, "Intercomparison of permittivity measurements using the transmission/reflection method in 7-mm coaxial transmission lines," *IEEE Trans Microw Theory Tech*, vol. 42, no. 11, pp. 2063–2070, 1994, doi: 10.1109/22.330120.

[32] J. Sheen, "Comparisons of microwave dielectric property measurements by transmission/reflection techniques and resonance techniques," *Meas Sci Technol*, vol. 20, no. 4, p. 042001, Apr. 2009, doi: 10.1088/0957-0233/20/4/042001.

[33] J. D. Breeze, X. Aupi, and N. McN. Alford, "Ultralow loss polycrystalline alumina," *Appl Phys Lett*, vol. 81, no. 26, pp. 5021–5023, Dec. 2002, doi: 10.1063/1.1532553.

[34] David M. Pozar, *Microwave Engineering 2nd Edition*. New York: Wiley; 2nd edition (August 12, 1997).

[35] K. WAKINO, M. MURATA, and H. TAMURA, "Far Infrared Reflection Spectra of Ba(Zn,Ta)O_3-$BaZrO_3$ Dielectric Resonator Material," *Journal of the American Ceramic Society*, vol. 69, no. 1, pp. 34–37, Jan. 1986, doi: 10.1111/j.1151-2916.1986.tb04689.x.

[36] W. M. Haynes, D. R. Lide, and T. J. Bruno, Eds., *CRC Handbook of Chemistry and Physics*. CRC Press, 2016. doi: 10.1201/9781315380476.

[37] W. Martienssen and H. Warlimont, Eds., *Springer Handbook of Condensed Matter and Materials Data*. Springer Berlin Heidelberg, 2005. doi: 10.1007/3-540-30437-1.

[38] N. McN. Alford and S. J. Penn, "Sintered alumina with low dielectric loss," *J Appl Phys*, vol. 80, no. 10, pp. 5895–5898, Nov. 1996, doi: 10.1063/1.363584.

[39] D. Brandon and W. D. Kaplan, *Microstructural Characterization of Materials*. Wiley, 2008. doi: 10.1002/9780470727133.

[40] Y. Xie, D. Kocaefe, Y. Kocaefe, J. Cheng, and W. Liu, "The Effect of Novel Synthetic Methods and Parameters Control on Morphology of Nano-alumina Particles," *Nanoscale Res Lett*, vol. 11, no. 1, p. 259, Dec. 2016, doi: 10.1186/s11671-016-1472-z.

[41] S. Kang, *Sintering: Densification, Grain Growth & Microstructure*. 2005.

[42] R. D. BAGLEY, I. B. CUTLER, and D. L. JOHNSON, "Effect of TiO2 on Initial Sintering of Al2O3," *Journal of the American Ceramic Society*, vol. 53, no. 3, pp. 136–141, Mar. 1970, doi: 10.1111/j.1151-2916.1970.tb12055.x.

[43] A. M. Abyzov, "Aluminum Oxide and Alumina Ceramics (review). Part 1. Properties of Al2O3 and Commercial Production of Dispersed Al2O3," *Refractories and Industrial Ceramics*, vol. 60, no. 1, pp. 24–32, May 2019, doi: 10.1007/s11148-019-00304-2.

[44] J. Zheng, X. Hu, Z. Ren, X. Xue, and K. Chou, "Solid-state Reaction Studies in Al2O3–TiO2 System by Diffusion Couple Method," *ISIJ International*, vol. 57, no. 10, pp. 1762–1766, 2017, doi: 10.2355/isijinternational.ISIJINT-2017-042.

[45] B. FREUDENBERG and A. MOCELLIN, "Aluminum Titanate Formation by Solid-State Reaction of Coarse Al_2O_3 and TiO_2 Powders," *Journal of the American Ceramic Society*, vol. 71, no. 1, pp. 22–28, Jan. 1988, doi: 10.1111/j.1151-2916.1988.tb05755.x.

[46] H. J. Thomas and R. Stevens, "Aluminium titanate: a literature review. I: Microcracking phenomena," *British ceramic. Transactions and journal*, vol. 88, pp. 144–151, 1989, [Online]. Available: https://api.semanticscholar.org/CorpusID:137874220

[47] C. Greskovich and V. S. Stubican, "Interdiffusion studies in the system MgO-Cr2O3," *Journal of Physics and Chemistry of Solids*, vol. 30, no. 4, pp. 909–917, Apr. 1969, doi: 10.1016/0022-3697(69)90288-1.

[48] W. P. Whitney and V. S. Stubican, "Interdiffusion studies in the system MgO Al2O3," *Journal of Physics and Chemistry of Solids*, vol. 32, no. 2, pp. 305–312, Jan. 1971, doi: 10.1016/0022-3697(71)90015-1.

[49] P. Zhang, T. DebRoy, and S. Seetharaman, “Interdiffusion in the MgO-Al2O3 spinel with or without some dopants,” *Metallurgical and Materials Transactions A*, vol. 27, no. 8, pp. 2105–2114, Aug. 1996, doi: 10.1007/BF02651865.

[50] Z. Ren, X. Hu, S. Li, X. Xue, and K. Chou, “Interdiffusion in the Fe2O3-TiO2 system,” *International Journal of Minerals, Metallurgy, and Materials*, vol. 20, no. 3, pp. 273–278, Mar. 2013, doi: 10.1007/s12613-013-0723-6.

[51] M. Sathiyakumar and F. D. Gnanam, “Influence of MnO and TiO2 additives on density, microstructure and mechanical properties of Al2O3,” *Ceram Int*, vol. 28, no. 2, pp. 195–200, Jan. 2002, doi: 10.1016/S0272-8842(01)00077-3.

[52] A. Khaskhoussi, L. Calabrese, J. Bouaziz, and E. Proverbio, “Effect of TiO2 addition on microstructure of zirconia/alumina sintered ceramics,” *Ceram Int*, vol. 43, no. 13, pp. 10392–10402, Sep. 2017, doi: 10.1016/j.ceramint.2017.05.074.

[53] K. Fukuda and R. K. Awai, “Microwave Characteristics of TiO_2-Bi_2O_3 Dielectric Resonator,” *Jpn J Appl Phys*, vol. 32, no. 10R, p. 4584, Oct. 1993, doi: 10.1143/JJAP.32.4584.

[54] Y. Ohishi, Y. Miyauchi, H. Ohsato, and K. Kakimoto, “Controlled Temperature Coefficient of Resonant Frequency of Al_2O_3-TiO_2 Ceramics by Annealing Treatment,” *Jpn J Appl Phys*, vol. 43, no. 6A, p. L749, Jun. 2004, doi: 10.1143/JJAP.43.L749.

[55] R. V. B. Campos, C. L. Bezerra, L. N. L. Oliveira, D. X. Gouveia, M. A. S. Silva, and A. S. B. Sombra, “A Study of the Dielectric Properties of Al2O3–TiO2 Composite in the Microwave and RF Regions,” *J Electron Mater*, vol. 44, no. 11, pp. 4220–4226, Nov. 2015, doi: 10.1007/s11664-015-3958-3.

[56] J. J. Gulicovski, L. S. Čerović, and S. K. Milonjić, “Point of Zero Charge and Isoelectric Point of Alumina,” *Materials and Manufacturing Processes*, vol. 23, no. 6, pp. 615–619, Jul. 2008, doi: 10.1080/10426910802160668.

[57] J. S. Reed, F. Matsrialwiseonschaft, and D. H. Darmstadt, “Introduction to the Principles of Ceramic Processing,” 1988.

[58] K. J. W. Atkinson, R. W. Grimes, M. R. Levy, Z. L. Coull, and T. English, “Accommodation of impurities in α-Al2O3, α-Cr2O3 and α-Fe2O3,” *J Eur Ceram Soc*, vol. 23, no. 16, pp. 3059–3070, Dec. 2003, doi: 10.1016/S0955-2219(03)00101-8.

[59] R. W. Grimes, “Solution of MgO, CaO, and TiO_2 in α-AI_2O_3,” *Journal of the American Ceramic Society*, vol. 77, no. 2, pp. 378–384, Feb. 1994, doi: 10.1111/j.1151-2916.1994.tb07005.x.

[60] S. O. Nelson, “Density-Permittivity Relationships for Powdered and Granular Materials,” *IEEE Trans Instrum Meas*, vol. 54, no. 5, pp. 2033–2040, Oct. 2005, doi: 10.1109/TIM.2005.853346.

[61] H.-J. Shih, Y.-C. Lee, Y.-D. Li, and C.-T. Yang, “Effect of Nb2O5 doping on low-temperature sintering of TiO2-Al2O3 ceramics,” *Open Ceramics*, vol. 19, p. 100635, Sep. 2024, doi: 10.1016/j.oceram.2024.100635.

[62] Y. Ohishi, Y. Miyauchi, K.-I. Kakimoto, and H. Ohsato, “Microwave Dielectric Properties of Al_2O_3-TiO_2 Improved by Addition of ZnO,” *Ferroelectrics*, vol. 327, no. 1, pp. 27–31, Oct. 2005, doi: 10.1080/00150190500315384.

[63] S. J. Bennison and M. P. Harmer, “Effect of MgO Solute on the Kinetics of Grain Growth in $A1_2O_3$,” *Journal of the American Ceramic Society*, vol. 66, no. 5, May 1983, doi: 10.1111/j.1151-2916.1983.tb10065.x.

[64] S. J. Bennison and M. P. Harmer, “Effect of Magnesia Solute on Surface Diffusion in Sapphire and the Role-of Magnesia in the Sintering of Alumina,” *Journal of the American Ceramic Society*, vol. 73, no. 4, pp. 833–837, Apr. 1990, doi: 10.1111/j.1151-2916.1990.tb05122.x.

[65] A. H. HEUER, “The Role of MgO in the Sintering of Alumina,” *Journal of the American Ceramic Society*, vol. 62, no. 5–6, pp. 317–318, May 1979, doi: 10.1111/j.1151-2916.1979.tb09496.x.

[66] E. R. WINKLER, J. F. SARVER, and I. B. CUTLER, “Solid Solution of Titanium Dioxide in Aluminum Oxide,” *Journal of the American Ceramic Society*, vol. 49, no. 12, pp. 634–637, Dec. 1966, doi: 10.1111/j.1151-2916.1966.tb13189.x.

[67] K. A. BERRY and M. P. HARMER, “Effect of MgO Solute on Microstructure Development in Al_2O_3,” *Journal of the American Ceramic Society*, vol. 69, no. 2, pp. 143–149, Feb. 1986, doi: 10.1111/j.1151-2916.1986.tb04719.x.

חקירת המאפיינים הדיאלקטריים והמיקרו-מבנה של קרמיקת מיקרוגל Al2O3-TiO2

חיבור על מחקר

לשם מילוי חלקי של הדרישות לקבלת התואר מגיסטר למדעים בהנדסת חומרים

יוטינג ש'יאו

הוגש לסנט הטכניון – מכון טכנולוגי לישראל

כסלו תשפ"ה חיפה דצמבר 2024